

I. PINHOLE DIFFRACTION SIMULATIONS

2

EUV Pinhole Diffraction

2.1 INTRODUCTION	8
2.1.1 Motivation of the Numerical Simulation	
2.2 MODELING THE ELECTROMAGNETIC FIELD	9
2.2.1 Calculating the Field in the Vicinity of the Pinhole	
2.2.2 Propagation to <i>Far-Field</i>	
2.3 THE DIFFRACTED WAVEFRONT	13
2.3.1 Simple Theory — The Airy Pattern	
2.3.2 Uniform and Conical Bore	
2.3.3 Elliptical Bore	
2.4 INTENSITY UNIFORMITY	18
2.5 ERROR ANALYSIS	19
2.6 CONCLUSION	21

2.1 INTRODUCTION

The central principle of the EUV point diffraction interferometers is the generation of the reference wavefront by pinhole diffraction. Both accuracy and precision rely on the spherical quality of the diffracted wavefront across the numerical aperture of measurement. A broad assumption may be made that for a sufficiently small pinhole, a spherical wavefront of arbitrary quality may be achieved over a given numerical aperture. However, such an assumption is difficult to justify for an experimental, and necessarily imperfect, pinhole in a highly absorptive, thick membrane subject to a plane-polarized incident electric field of non-uniform intensity.

In principle, detailed knowledge of the electromagnetic field emerging from the pinhole membrane would enable the prediction of non-spherical components in the diffracted wavefront phase and allow estimation of the measurement accuracy limits. The goal of this section is to assess the results of a first-principles simulation of the pinhole-diffracted reference wavefront, to guide the selection of the appropriate pinhole size and characteristics of the experimental interferometer.

While the simplifying assumptions of this simulation do overlook several experimental conditions (non-ideal pinhole shapes, spatial variation of the incident electric field, etc.), this work lays the foundation for further research and more detailed analysis performed utilizing the rapidly increasing capacity and availability of computing power. These early results may portray an optimistic view of the minimum required pinhole size for EUV interferometry: only careful experimental research can truly establish a maximum allowable pinhole size or qualify an individual pinhole for a given application and desired accuracy.

2.1.1 *Motivation of the Numerical Simulation*

Several methods have been developed to study diffraction from a variety of aperture shapes with various boundary conditions (Cerjan 1994, Born and Wolf 1980), yet no general analytical treatment addresses diffraction through pinholes in a highly absorptive medium with the range of non-ideal shapes that serve as reasonable physical models for the experimental pinholes used in EUV point diffraction interferometry near 13 nm wavelength (Goldberg et al. 1996). The introduction of the three-dimensional pinhole structure and inclusion of the polarization of incident light motivate the use of numerical solutions based on detailed simulations of the vector electromagnetic field in the vicinity of the pinhole. This in itself presents an especially difficult challenge owing to the relatively large diameter of the pinholes in question ($3-15 \lambda$) and the polarization-dependent absorptive boundary conditions at the membrane interfaces.

Beyond rigorous numerical solution of Maxwell's equations in the domain containing the pinhole, no analytic treatment is sufficiently versatile to accommodate the irregular pinhole shape models that serve as approximations to the actual shape of the experimental pinholes. Determination of the complete electromagnetic field in the vicinity of the pinhole was performed in this study for a variety of pinhole

geometry models using TEMPEST 3D (Wong and Neureuther 1995). Several pinhole models with cylindrical and elliptical cross-sections were considered in the studies described in this chapter. These calculations set an upper limit to the allowable pinhole diameters necessary to achieve a reference wavefront of a given quality in an ideal system.

All of the TEMPEST 3D calculations were performed in 1995 on a CM-5 connection machine. Typically, these simulations utilized 128 parallel processors and 870 MB of RAM, requiring approximately five minutes of CPU time. At the time these simulations were performed, the large simulation domains necessitated the use of a super-computer and restricted the simulations to a narrow cross-sectional area containing the open pinholes. The author notes that at present such computing power (aside from the number of processors) is becoming available on desktop workstations.

2.2 MODELING THE ELECTROMAGNETIC FIELD

Pinholes with diameters ranging from 50-150 nm (~ 3 - 11λ , at $\lambda \approx 13$ nm), fabricated by electron beam lithography in a highly absorptive cobalt membrane approximately 90 nm ($\sim 7 \lambda$) thick (Spallas et al. 1995), are considered in this study because they are suitable for testing optical systems with NA around 0.1 near 13 nm wavelength. The three-dimensional electromagnetic field in the vicinity of the pinhole was calculated using TEMPEST 3D, a time-domain, vector electromagnetic field simulation computer program. Once the field has been calculated at the exit-side of the pinhole membrane, the reference wavefront is calculated using a simple vacuum-propagation model incorporating the Fresnel-Kirchoff approximation for far-field diffraction.

2.2.1 Calculating the Field in the Vicinity of the Pinhole

Calculations are performed on a range of pinhole geometry models, including cylindrical and conical pinholes and elliptical pinholes of uniform cross-section. Figure 1 shows the four pinhole-bore models studied here. To simplify the models, variations of the field incident on the pinhole are neglected: across the small simulation domain, uniform, normally incident plane-wave illumination with linear polarization along the x -axis is assumed. Experimentally, however, the electric field may vary over an extremely small

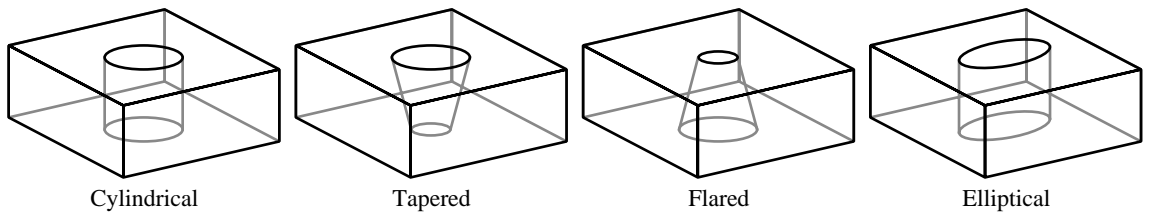


Figure 1. A representation of the four pinhole shape models used in the TEMPEST 3-D simulations. The pinholes range from 50 — 150 nm diameter. The walls of the sloped pinholes (tapered and flared) are angled at 10° to the vertical. The two-fold symmetry of these models is exploited to increase the simulation domain size.

Table 1. Parameters of the pinhole simulations

wavelength	$\lambda = 13.55 \text{ nm}$ (91.5 eV)
illumination	uniform plane wave, normal incidence, plane polarized
simulation domain size	$230.6 \text{ nm} \times 230.6 \text{ nm} \times 115.2 \text{ nm} = 17 \lambda \times 17 \lambda \times 8.5 \lambda$, periodic in x and y
simulation nodes	uniform, $\lambda/15$ spacing, 2×10^6 total nodes, exploiting two-fold symmetry
pinhole diameters	50 nm – 150 nm
cobalt membrane	thickness, 90 nm = 6.64λ ; density, 8.9 g/cm ³
index of refraction	$n \equiv 1 - \delta + i\beta = 1 - 0.0659 + 0.0657i = 0.9341 + 0.0657i$

spatial scale, rendering suspect the uniform-illumination assumption. This is especially true for large pinholes, and for those displaced significantly from the center of the focal pattern. Thus the pinhole size conditions described herein set a *lower limit* for the magnitude of aberrations that should be expected from ideal plane-wave illumination.

Parameters of the simulation are listed in Table 1. The simulation domain, which exploits the two-fold symmetry of the pinhole models, contains a cobalt membrane in vacuum with a thin free-space layer above and below. TEMPEST 3D uses periodic boundary conditions in the x and y directions, thereby forming an infinite square array of *virtual* pinholes with center-to-center spacing of 230.6 nm for the parameters of interest. This periodicity is represented in Fig. 2(a). If the pinhole itself is symmetric about both the x - and y -axes, defined from the center of the pinhole (as is always the case in these simulations), then the domain size may be reduced by a factor four, as shown in Fig. 2(b). (It should be noted that recent versions of TEMPEST under development do not impose periodic boundary conditions. These advances were not available at the time this research was undertaken.)

The propagation of EUV light in cobalt is characterized by *rapid* extinction: the $1/e$ intensity transmission depth is 16.4 nm (1.21λ) at 13.55 nm wavelength, and the relative transmission through 90 nm is 4.1×10^{-3} . This rapid extinction is important to the separation distance between the pinholes of the peri-

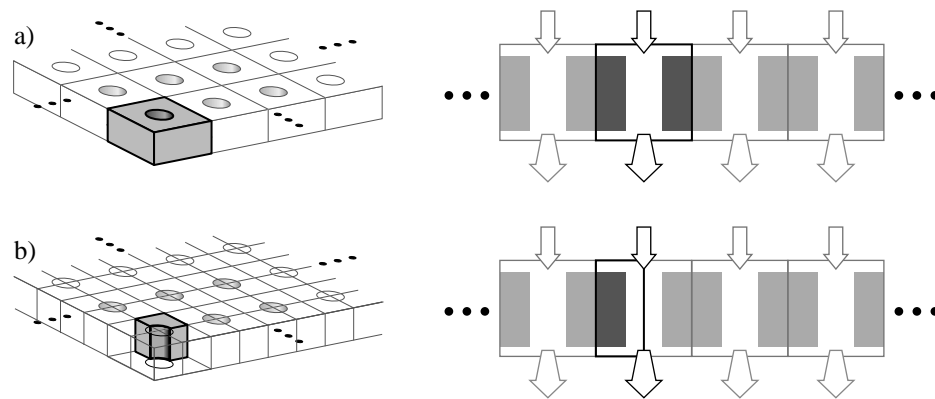


Figure 2. The three-dimensional TEMPEST simulation domain. (a) The inherent periodic boundary conditions create a virtual lattice containing the simulation domain. On the right is a cross section containing the pinhole axis. The limits of the simulation domain are outlined in black. (b) The simulations performed here exploit the two-fold symmetry of the pinhole models to enable the simulation of larger domains.

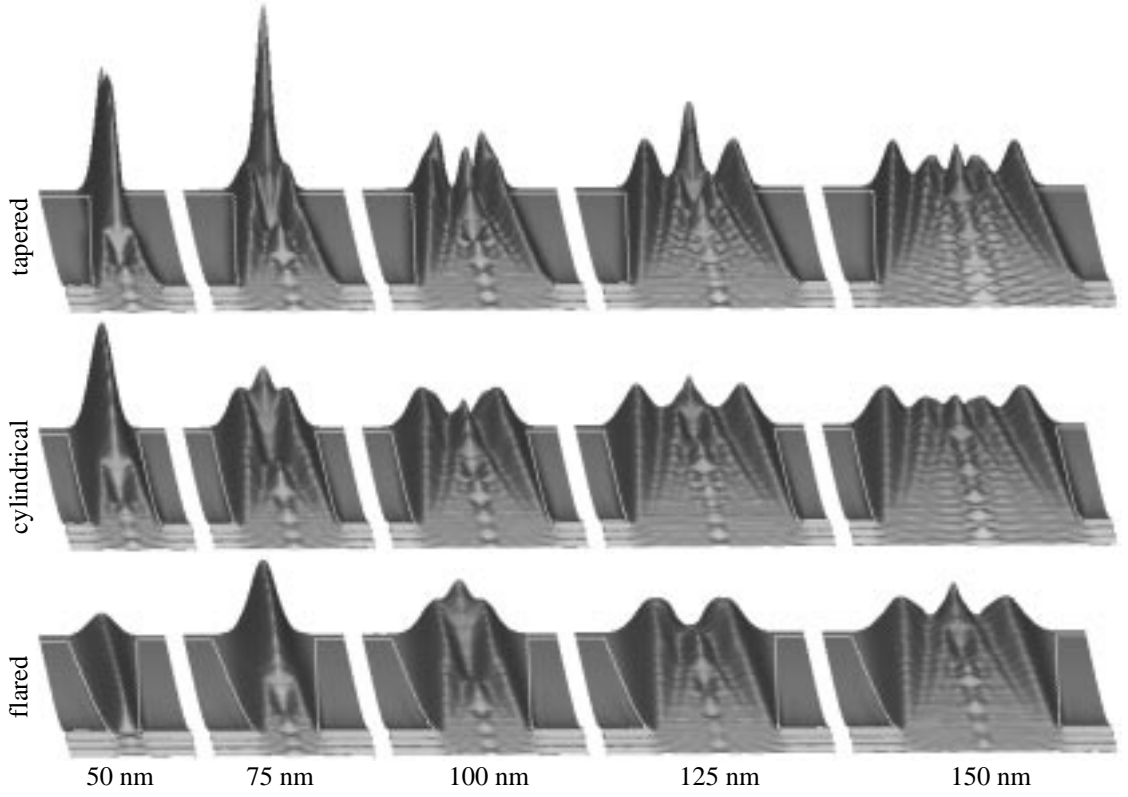


Figure 3. Calculated electric field intensity patterns showing diffraction within the pinhole and attenuation in the cobalt membrane. Surface heights represent the electric field intensity in a plane containing the axis of the pinhole and the direction of the electric field polarization. The light propagates from the bottom of each image to the top. White lines on the surfaces represent the boundaries of the cobalt.

odic domain. In order to consider the individual pinholes as isolated structures, the separation must be great enough to substantially reduce the contribution of overlapping fields from the neighboring *virtual* pinholes. Hence the rapid extinction makes this simulation possible.

A short distance away from the pinhole, light propagates through the material with characteristic exponential extinction:

$$I(x) = I_0 e^{-x/16.4 \text{ nm}}. \quad (1)$$

Within the open pinhole, a stationary diffraction pattern is formed. For pinholes of circular cross-section and various radii, the electric field is shown in Fig. 3. The figure shows only the cross section taken in the plane parallel with the polarization.

Polarization affects the propagation of light in the pinhole, and breaks the rotational cylindrical symmetry of the study. Along the walls of the pinhole (i.e. the interface), the electric field satisfies different boundary conditions in the different directions. The electric field polarized *parallel* to the boundary must be continuous across the interface, with a continuous first derivative in the direction normal to the boundary. Since the field inside the absorber is rapidly attenuated, this continuity requirement forces the parallel electric field to become nearly zero along the pinhole walls. The field polarized *perpendicular* to

the interface may be discontinuous, and is not necessarily small at the boundary.

This polarization dependence illustrates one main difference between scalar and vector solutions to pinhole diffraction. While it is true that for pinhole diameters many times larger than the wavelength, the contributions from the boundaries of the pinhole become negligible, this is certainly not the case for the pinholes of interest here. The difference between the parallel and perpendicular boundary orientations establishes a 2θ -dependence in the diffracted wavefront manifested as a small amount of *astigmatism* (the lowest-ordered 2θ -dependent aberration).

2.2.2 Propagation to Far-Field

Once the fields have been calculated and the field at the exit of the pinhole is known, the diffracted wavefronts are calculated by numerical propagation of the calculated electric field to a spherical surface, 10 cm away. Experimentally, this distance represents diffraction to the *far-field* and corresponds to the position of the detector in the EUV point diffraction interferometer and phase-shifting point diffraction interferometer described in this thesis. The x -polarized component of the electric field, calculated 2.7 nm ($\lambda/5$) below the cobalt membrane, is used as the *initial field* for the numerical propagation. In the absence of a y -polarized component, the x -polarized component of the electric field across the initial x - y plane is sufficient to completely and uniquely describe the propagated field (Clarke and Brown 1980). Furthermore, for relevance to interferometry the interference fringe pattern is generated by the interaction of like-polarized electric field components of the test and reference beams. The test wave here contains only x -polarized light, and therefore the presence of any y -polarized light in the reference beam would contribute only to the stationary background intensity. The propagation is performed with a two-dimensional Fourier transform that approximates the Fresnel-Kirchoff diffraction formula for far-field diffraction (Born and Wolf 1980).

In the pinhole simulation domain, the propagated *emergent* field may be described as the linear superposition of the *diffracted* field and the incident *uniform* field transmitted through the cobalt membrane. To isolate the diffracted field, a uniform (constant) component representing only the attenuated transmitted field is subtracted before the propagation was performed. This superposition and subtraction is illustrated in Fig. 4. Isolation of the diffracted field enables the imposition of the boundary condition that

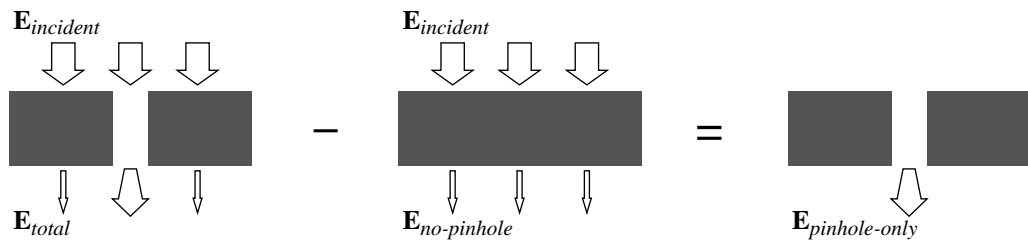


Figure 4. Strategy for the calculation of the diffracted wavefront from TEMPEST simulations. Superposition is used to isolate the diffracted wave from the wave transmitted in the absence of the pinhole. This subtraction is necessary to eliminate the contribution of the finite, square simulation domain cross-section.

the diffracted field becomes arbitrarily small away from the pinhole. As mentioned previously, the rapid extinction of all light not transmitted *through* the open pinhole allows the use of a relatively small domain size in these calculations.

2.3 THE DIFFRACTED WAVEFRONT

The Kirchoff model of scalar diffraction theory (Born and Wolf 1980) provides a first approximation to the far-field wavefront diffracted from the experimental pinhole.

2.3.1 Simple Theory — The Airy Pattern

Consider the diffraction of uniform, plane-wave illumination from a simple circular aperture in a planar screen. For a small aperture, in the far-field this is referred to as *Fraunhofer diffraction* (Goodman 1988:62). This simplified model predicts a spherical reference wavefront that covers the central portion of a diffracted *Airy pattern*, bounded by the first diffraction minimum.

A highly simplified model of the field emergent from a circular pinhole of diameter d is

$$t(\mathbf{r}) = \begin{cases} 1, & |\mathbf{r}| \leq d/2 \\ 0, & |\mathbf{r}| > d/2 \end{cases} . \quad (2)$$

Following Goodman (1988:48-54), the angular spectrum of the diffracted wavefront when the system is illuminated by a normally incident, monochromatic plane wave is calculable via Fourier-transform. Let $\boldsymbol{\alpha} \equiv (\alpha_x, \alpha_y)$ be direction cosines of the field in the x and y directions. The angular spectrum is

$$U(\boldsymbol{\alpha}/\lambda) = \int_{dA} t(\mathbf{r}) \exp\left[-\frac{2\pi i}{\lambda} \boldsymbol{\alpha} \cdot \mathbf{r}\right] d\mathbf{r} . \quad (3)$$

Taking advantage of the cylindrical symmetry of the problem, Eq. (3) can be solved using the Fourier-Bessel transform. The result is the familiar *Airy pattern*, named after its discoverer, G. B. Airy.

$$U(\boldsymbol{\alpha} / \lambda) = 2\pi \int_0^\infty t(r) J_0\left(\frac{2\pi}{\lambda} \alpha r\right) r dr = 2\pi \int_0^{d/2} J_0\left(\frac{2\pi}{\lambda} \alpha r\right) r dr = \frac{\lambda d}{2\alpha} J_1\left(\frac{\pi \alpha d}{\lambda}\right) . \quad (4)$$

The intensity is proportional to the aperture area:

$$I(\boldsymbol{\alpha} / \lambda) \propto \left(\frac{\lambda d}{2\alpha}\right)^2 J_1^2\left(\frac{\pi \alpha d}{\lambda}\right) . \quad (5)$$

The first diffraction minimum corresponds with the first zero of the Bessel function $J_1(x)$ at $x \approx 1.22 \pi \approx 3.83$. Hence, with θ as the polar angle,

$$\alpha \approx 1.22 \lambda/d \rightarrow \sin\theta \approx 1.22 \lambda/d . \quad (6)$$

To compare the *phase* of Eq. (4) with an ideal, spherical wavefront, notice that the expression is purely real. Changes in sign correspond to a π change of phase. Thus, by inspection, the phase of the Airy

Table 2. Maximum measurement NA based on an ideal Airy diffraction pattern producing a spherical reference wavefront within the first diffraction minimum.

d [nm]	50	75	100	125	150	175
NA	0.33	0.22	0.17	0.13	0.11	0.094

pattern relative to an ideal spherical wave ϕ_{Airy} is

$$\phi_{Airy} = \begin{cases} 0, & J_1(\pi\alpha d/\lambda) \geq 0 \\ \pi, & J_1(\pi\alpha d/\lambda) < 0 \end{cases} . \quad (7)$$

In this simple treatment, the phase of the diffracted wavefront is *perfect* over the central region of the pattern. The NA that is filled by this central region is

$$NA_{filled} \approx \sin\theta \approx 1.22 \lambda/d . \quad (8)$$

Calculations based on Eq. (8) are shown in Table 2.

In each TEMPEST simulation case, the phase of the diffracted wavefront is fit to a series of Zernike polynomials (see Chapter 15) over a range of NA angles. The four lowest-order polynomials that describe the displacement of the coordinate system from the wavefront center of curvature are removed from this analysis. Pinholes from which the remaining peak-to-valley (P-V) wavefront aberration is larger than 0.15λ are rejected from consideration in this study. This includes all pinholes larger than 150-nm in diameter.

2.3.2 Cylindrical and Conical Bore

In addition to a simple cylindrical bore, two conical bore models, tapered (narrower at the exit) and flared (wider at the exit), are studied in this chapter. For both of the conical models, the cone half-angle is 10° . The five pinhole diameters studied here are 50, 75, 100, 125, and 150 nm. Conical pinholes are labeled by their *maximum* diameters.

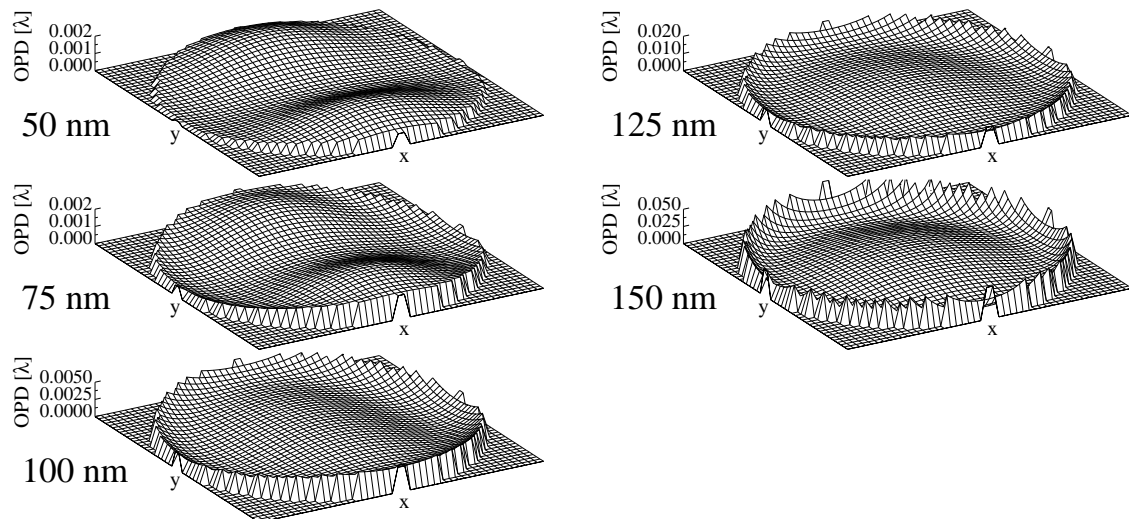


Figure 5. Calculated wavefronts diffracted by cylindrical pinholes. The optical path difference (OPD) between the diffracted wavefront and an ideal spherical wavefront is shown. The incident illumination is x -polarized. Note the changes in the z -axis scaling.

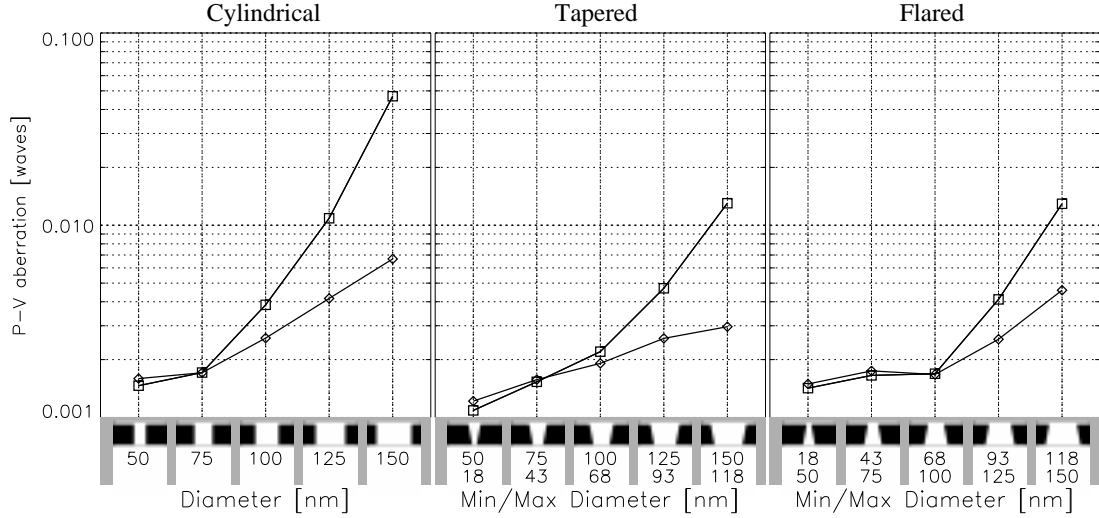


Figure 6. Calculated P-V wavefront aberrations within 0.08 (diamond symbol) and 0.1 (square symbol) NA for three pinhole bore shape models and five different diameters. Pinhole cross-sections, parallel to the polarization vector, are shown above the x-axis labels: black represents the cobalt membrane, white is empty space. Anomalous behavior is seen in the 50-nm-diameter pinholes where the astigmatic aberrations dominate the diffracted wavefronts and the 0.08 NA wavefront has a larger peak-to-valley error than the 0.1 NA wavefront when the defocus terms are subtracted.

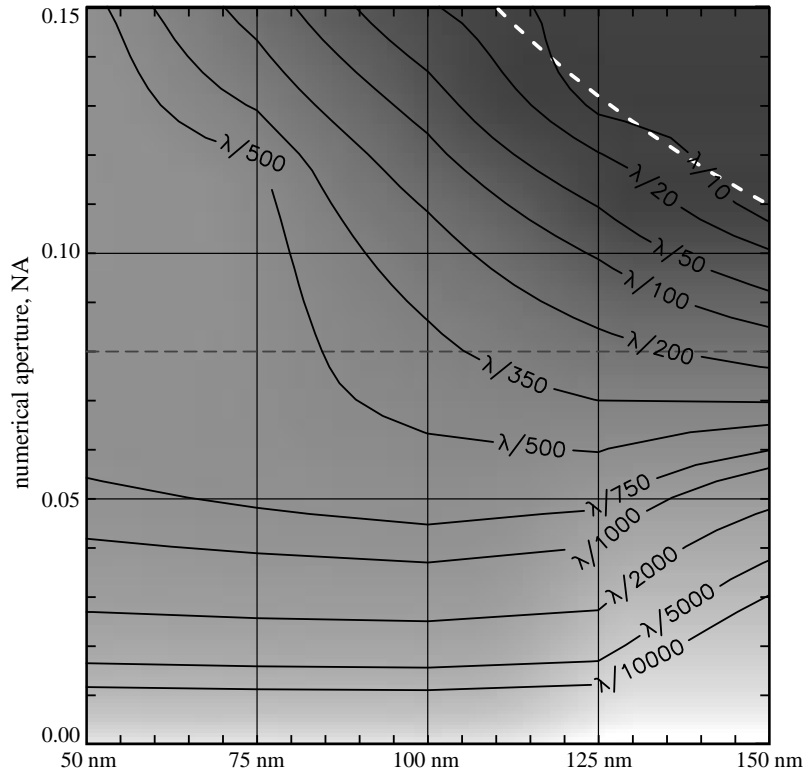


Figure 7. Calculated reference wavefront P-V aberration magnitude plotted as a function of pinhole diameter and numerical aperture for pinholes in the cylindrical bore model. Wavefronts are only calculated for the five labeled pinhole diameters; bi-cubic interpolation is used to generate the contours in the intermediate regions. The expected behavior of wavefront quality improving with reduction in pinhole size is demonstrated; however, anomalous behavior occurs where the pinholes are greater than 100 nm and NA is below 0.08. The cross-section for 0.08 NA is indicated by a dark dashed line. The dashed white line indicates the maximum NA of the spherical wavefront predicted by the simple Airy diffraction formula, $NA = 1.22 \lambda/d$.

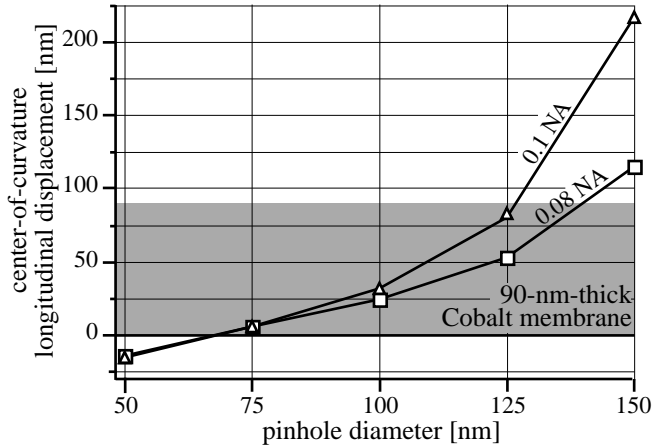


Figure 8. Longitudinal change in the center-of-curvature of the wavefront diffracted by cylindrical pinholes of five different diameters. The center-of-curvature is determined from the defocus term in a best-fit Zernike polynomial series representation of the reference wavefront. The presence of higher-ordered aberrations creates a dependence of the defocus on the NA of measurement; this is especially evident for the 150-nm-diameter pinhole. Longitudinal position is measured from the bottom (exit-side) of the cobalt membrane; positive position values indicate that the center-of-curvature lies *within* the pinhole.

Calculated wavefronts diffracted by the cylindrical pinholes are plotted in Fig. 5 with the piston, tilt, and defocus components removed. Wavefronts diffracted by the two smallest pinholes reveal a small astigmatic component, while the largest pinholes diffract wavefronts dominated by rotationally symmetric aberrations.

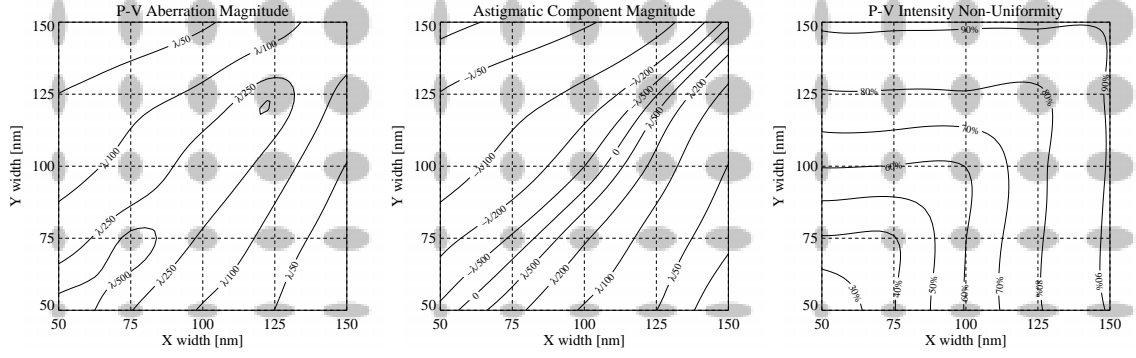
The calculated P-V wavefront aberration magnitudes are plotted in Figs. 6 and 7 for each of the pinhole bore shapes and diameters studied. Within this range, the P-V aberration magnitude is an increasing function of the pinhole size. The dominant wavefront aberration components for the larger pinholes are rotationally symmetric (spherical aberration). However, a small astigmatic ($\cos 2\theta$) component, less than 0.02λ P-V, is present in each diffracted wavefront.

There is no significant qualitative difference between the wavefronts diffracted by the cylindrical and the conical pinhole models. In general, each conical pinhole diffracts a reference wavefront that is similar to a wave diffracted from a cylindrical pinhole of diameter between the minimum and maximum conical diameter.

As the raw wavefront data is analyzed, defocus, a rotationally-symmetric aberration component of order r^2 , is typically the dominant aberration component. Defocus, however, arises from the arbitrary position of the origin of the coordinate system (just below the pinhole membrane) used in the calculation. Experimentally, the defocus is determined by the relative longitudinal positions of the test beam and the membrane containing the reference pinhole. There exists one point along the axis of symmetry which may be called the center-of-curvature of the diffracted wavefront. This point, for which the best-fit defocus is identically zero, occurs somewhere in the vicinity of the reference pinhole. The next-higher rotationally-symmetric aberration component is spherical aberration, of order r^4 . Due to the r^2 dependence of the defocus magnitude and presence of higher-order aberrations, the best-fit amount of defocus in an arbitrary reference wavefront depends strongly on the NA of measurement.

One characteristic observable in the data is a shift of the longitudinal position of the center-of-curvature with changing pinhole size, shown in Fig. 8. This effect is an important contributor to the astigmat-

NA = 0.08



NA = 0.10

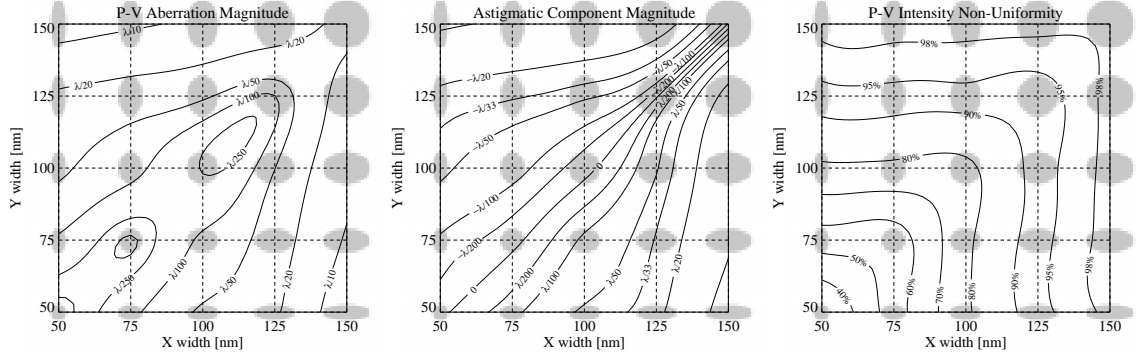


Figure 9. Calculated characteristics of the reference wavefronts diffracted from elliptical pinholes into 0.08 and 0.10 NA. With the position-dependent wavefront components removed, the residual P-V wavefront aberrations, the amplitude of the astigmatic ($\cos 2\theta$) components, and the intensity non-uniformity are shown. The 25 pinhole shapes are shown in grey behind the appropriate locations on the plots; intermediate points are based on a minimum-curvature surface interpolation and are thus not verified by the simulation. Pinhole ellipticity and the x -direction polarization of the incident light both introduce a small amount of astigmatism into the diffracted wavefronts. Note that in the top-center plot, the unlabeled contours are $\lambda/33$. In the bottom-center plot, the unlabeled contour is $\lambda/10$.

ic wavefront found from *elliptical* pinholes, discussed in the following section.

The asymmetric wavefront components in diffraction from *circular* pinholes come from the polarization of the incident field. As stated earlier, electric field components parallel and perpendicular to the vertical walls of the pinhole satisfy different boundary conditions. The field emerging from the pinhole is not rotationally symmetric, but contains *astigmatic* components.

2.3.3 Elliptical Bore

A series of simulations was conducted to investigate the effect of elliptical pinhole cross-sections on the diffracted wavefront. Several of the relevant reference wave parameters are shown in Fig. 9, for 25 width and ellipticity combinations at 0.08 and 0.1 NA.

From elliptical pinholes, the diffracted reference wavefront can contain a significant amount of astigmatism. In the previous section, the dependence of the longitudinal position of the center-of-curvature with respect to the pinhole size was discussed; this effect is manifest in the rotationally-symmetric defocus term. Here, where the pinholes are elliptical, the horizontal and vertical *centers-of-curvature*

occur at different longitudinal positions; the r^2 defocus term then takes on a 2θ dependence and astigmatism is introduced into the diffracted wavefronts. Furthermore, regarding the higher-ordered aberrations, the elliptical pinhole wavefronts show greater aberration magnitudes in the direction of the pinholes' major-axis, leading to an additional source of astigmatism. Figure 9 shows the P-V aberration magnitude and the magnitude of these astigmatic components, in addition to the intensity non-uniformity discussed in the following section. Since the astigmatic term depends on $\cos 2\theta$, a negative sign of the coefficient simply indicates rotation by 90° .

2.4 INTENSITY UNIFORMITY

Separate from the wavefront phase, an important consideration for the quality of the reference wavefront is the intensity uniformity across the NA of measurement. In an ideal Airy pattern, for example, although the wavefront *phase* is that of an ideal spherical wavefront, the *intensity* varies monotonically from its peak at the center of the pattern to zero at the first diffraction minimum. Since the signal-to-noise of the measurement is related to fringe contrast, and fringe contrast depends on the relative intensities of the test and reference waves, the uniformity of the reference wave must be taken into consideration in the selection of the appropriate reference pinhole diameter.

To evaluate the uniformity of the pinhole-diffracted reference wave, define a non-uniformity

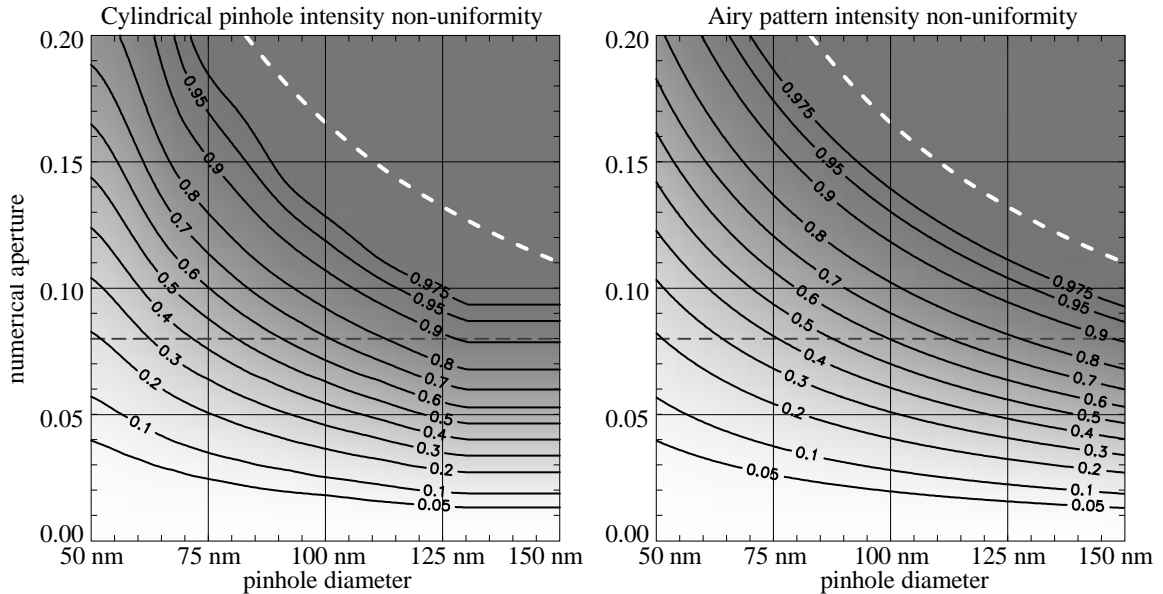


Figure 10. The intensity non-uniformity of the diffracted wavefronts in the cylindrical bore model, calculated for a range of pinhole diameters and numerical apertures and compared with the features of the Airy pattern. Pinhole-diffracted reference waves cannot uniformly illuminate arbitrarily large apertures. Non-uniformity from the radial decrease in intensity ultimately affects interferogram fringe contrast. The dashed dark line indicates 0.08 NA. The dashed white line indicates the angle of the first Airy diffraction minimum where, in the simple theory, the non-uniformity is one.

parameter v as

$$v \equiv 1 - \frac{I_{min}}{I_{max}}. \quad (9)$$

By this definition, when the reference wavefront is perfectly uniform, I_{min} equals I_{max} , and v is zero. On the other hand, if the reference wave intensity falls to zero within the NA, then I_{min} equals zero, and v is one.

Based on the TEMPEST 3D calculations for the cylindrical-bore pinhole model, discussed in Section 2.3.2, Fig. 10 shows the reference wave intensity non-uniformity as a function of pinhole diameter and NA. The TEMPEST compares very closely with the simple Airy model, also shown. The calculation reveals that a reasonable reference wave non-uniformity of 30% at 0.08 NA requires a sub-75-nm-diameter pinhole, and at 0.1 NA requires a sub-50-nm pinhole. These are very challenging requirements.

2.5 ERROR ANALYSIS

The uncertainty of the phase or intensity of the diffracted waves can be estimated using information about the simulation method and separately, using data from the calculations. The simulation convergence requirements, the electric-field data, and a separately calculated secondary data set are here used to place upper limits on the magnitude of the uncertainties.

One cause of uncertainty is the finite lateral size of the simulation domain. An estimate of the total power *outside* of the simulation domain provides an upper-limit to this uncertainty. Based on the field magnitude at the edge of the domain and the rate of field attenuation away from the pinhole, the uncertainty upper-limit in the diffracted field is estimated to be not more than 10^{-4} based on a unit amplitude incident field. This field uncertainty translates to 10^{-4} radians or $\sim 2 \times 10^{-5}$ waves of phase uncertainty. Attenuation in the membrane makes the contributions from the adjacent virtual pinholes in the periodic simulation domain even smaller than this level. Further study is required to fully characterize the uncertainty introduced by the small domain size.

The TEMPEST 3D electromagnetic-field simulation utilizes an iterative approach to compute the fields within the domain. Convergence or *steady-state* is achieved when three successive iterations agree to within a given *absolute* tolerance ϵ . Only a small subset of the domain points are used in the convergence testing. An alternate convergence scheme using the *relative* field magnitude may be more appropriate for simulations such as this, where the field magnitude varies substantially from one region to the next. Furthermore, convergence tests across the entire domain or a full cross-section of it would improve confidence in the results. Such strategies were not implemented in this version of the TEMPEST program.

With a unit amplitude input electric field, the convergence parameter ϵ is set equal to 0.01. Smaller values require much longer processing time, making their use infeasible for the breadth of experiments

performed. Yet this value of ϵ renders the uncertainty in each point to be as large as 0.01. With the calculation of the first-quadrant field *unfolded* to all four quadrants, there are 255×255 or 65,025 lateral nodes in the domain. Since the diffracted wave is calculated via discrete Fourier-transform, the errors propagate linearly into the wavefront measurement. That is, any component of the Fourier-spectrum is calculated by a simple summation of the field in the image-plane. The maximum uncertainty (without any scaling coefficient) in that measurement is $65,025 * \epsilon \approx 650$. The figure of merit is the ratio of this maximum uncertainty to the amplitude of the diffracted wave: this value dictates the *maximum* phase error. For the five pinhole sizes ranging from 50 to 150 nm {50, 75, 100, 125, 150 nm} the unscaled peak amplitudes of the diffracted waves are {5503, 8222, 12044, 17460, 23013}, making the maximum uncertainty at the peaks {11%, 8%, 5.4%, 3.7%, 2.8%}. Following this argument, the uncertainties increase away from the peak because of the decrease in the diffracted wave's amplitude with angle.

Uncertainty in the complex field amplitude translates directly into maximum uncertainties in the phase. Based on the vector addition of the peak calculated field amplitude with the uncertainty (having unknown phase), the maximum net phase error is {0.11, 0.08, 0.054, 0.037, 0.028} radians, or {0.018, 0.013, 0.009, 0.006, 0.004} waves or $\{\lambda/56, \lambda/77, \lambda/116, \lambda/170, \lambda/224\}$.

In practice, these maximum uncertainty values are *much* larger than the actual errors in the calculation. Because of the absorptive membrane, most of the field amplitudes at the exit-side of the simulation domain are smaller than 0.01, the error tolerance, yet the fields are well-behaved and are reliable to a much higher accuracy.

One secondary estimate of the uncertainties comes from consideration of the y-polarized field. The illuminating electric field is polarized only in the x-direction and the material contains no polarization-rotating bi-refrignence. The presence of a y-polarized field comes from very small glancing-incidence reflections within the pinhole and from numerical errors accrued during the calculation of various vector field curls and divergences. For this reason, the errors should not be larger than the amplitude of the y-polarized components.

Similar to before, since a discrete Fourier-transform is used to calculate the diffracted wave, the sum of the absolute values of the y-polarized field amplitudes at the exit-side of the domain can be used to estimate the error. Here, the field totals for the three smallest pinholes are {60, 34, 19}, meaning uncertainties at the peaks of {0.3%, 0.4%, 0.5%} relative to the peak amplitudes stated previously. Because of the intensity fall-off, uncertainties at the maximum angles within the diffracted wavefront are on the order of twice these values. The amplitude uncertainties relate to phase uncertainties of $\{4.8 \times 10^{-4}, 6.4 \times 10^{-4}, 8.0 \times 10^{-4}\}$ waves, or $\{\lambda/2100, \lambda/1570, \lambda/1260\}$.

It is difficult to judge the accuracy or reliability of these calculations well below $\lambda/100$ or $\lambda/500$.

Further research could be used to clarify some outstanding issues: how do the diffracted waves depend on the domain size, the number of nodes per wavelength, the absolute error tolerance ϵ , single- versus double-precision calculations, etc.? In the absence of such tests, these results must stand as they are, awaiting further verification.

2.6 CONCLUSION

Calculated EUV wavefronts diffracted into 0.08 and 0.1 NA by 50 to 150-nm pinholes in a cobalt membrane show aberrations that increase as a function of pinhole size. Even in the presence of a slightly conical bore or an elliptical cross-section, the diffracted wavefronts are spherical to within 0.01 waves ($\lambda/100$) from 125-nm pinholes and within 0.002 waves ($\lambda/500$) from sub-75-nm circular pinholes. Both polarization and pinhole ellipticity introduce astigmatic components into the diffracted wavefront. Polarization contributes astigmatism due to the rotational-symmetry-breaking boundary conditions. Since the longitudinal center-of-curvature varies as a function of pinhole diameter, elliptical pinholes with different diameters along the major and minor axes generate astigmatism by a different mechanism.

The intensity uniformity of the diffracted waves is an essential consideration for evaluating the quality of the reference wavefront. Experimentally, the desire for intensity uniformity places a separate restriction on pinhole size from the phase-uniformity requirement. Within these simulations it is shown that the sub-75-nm pinholes are capable of producing non-uniformities below 30% for 0.08 NA measurements, while sub-50-nm pinholes are required for the same non-uniformity at 0.1 NA. These results closely follow the predictions of the simple Airy-pattern from the Kirchhoff diffraction model.

To the extent that these pinhole models correctly represent experimental conditions, measurements of aberrated spherical wavefronts using EUV point diffraction interferometry may be limited to an accuracy of a few thousandths of a wavelength when pinholes as small as 50 nm are used — substantially smaller than the diffraction-limited resolution of the test optics.

II. THE CONVENTIONAL PDI

3

The Point Diffraction Interferometer

3.1 INTRODUCTION AND MOTIVATION	26
3.2 THE CONVENTIONAL PDI	26
3.3 COMPONENTS OF THE EXPERIMENTAL SYSTEM	27
3.3.1 EUV Fresnel Zoneplates	
3.3.2 Undulator Light Source and ALS Beamline 9.0.1	
3.3.3 Pinholes	
3.3.4 Stages	
3.3.5 Other Components	
3.4 THE TEST WAVE: FRESNEL ZONEPLATE DIFFRACTION PATTERN	33
3.5 THE REFERENCE WAVE	33
3.5.1 Pinhole Diffraction	
3.5.2 <i>In Situ</i> Quality Assessment	
3.5.2.1 Zeros of Fringe Visibility	
3.5.2.2 Fringe Forking	
3.5.2.3 Contrast Variation	
3.5.2.4 Contamination	
3.6 PDI EXPERIMENTS: FRESNEL ZONEPLATE TESTING	37
3.6.1 Raw Data	
3.6.2 Wavefront Analysis	
3.7 CONCLUSION	42
3.8 NOTE: THE CONTRIBUTION OF CONTAMINATION TO WAVEFRONT MEASUREMENTS	43

3.1 INTRODUCTION

The first prototype implementation of the EUV point diffraction interferometer (PDI) was dedicated to the development of high-accuracy EUV interferometric capability, and to the investigation of high-resolution Fresnel zoneplate lenses. The experiments and measurements described in this chapter detail the progress made toward those goals.

Experiments related to the investigation of zoneplate aberrations were conducted between August 1994 and August 1995. These experiments revealed the nearly diffraction-limited quality of the low-spatial-frequency wavefront aberrations (Goldberg et al. 1995a, 1995b). Mid- and high-spatial frequency aberrations were observable in the measured intensity profiles (Tejnil et al. 1996b).

As a demonstration experiment, the EUV interferometry performed on Fresnel zoneplate lenses was the first critical step toward the development of more sophisticated measurement techniques. Ultimately, the uncertainties in the measurements were on the same order as the wavefront aberrations that were found, and the success of the measurements was limited by a range of experimental issues. However, a great number of concrete lessons were learned; the significant problems were identified and later overcome.

This chapter details the theory and use of the EUV PDI and describes the experimental system. The characterization of a Fresnel zoneplate lens is presented. Development of this prototype EUV interferometer led to a superior interferometer design concept, the PS/PDI, which is the subject of Part III of this thesis. Before the measurement goals for the zoneplate lenses could be achieved, the PS/PDI was applied to the measurement of lithographic reflective optical systems.

3.2 THE CONVENTIONAL PDI

The PDI was first described by Linnik (1933) and later by Smartt and Steel (1975) as a simple, common-path, wavefront-splitting interferometer well-suited for applications in X-ray optics, where conventional amplitude-splitting interferometer designs are not easily implemented. The PDI has previously been used successfully in a number of short wavelength applications (Speer et al. 1979, Mrowka and Speer 1981). The interferometer, shown in Fig. 1, consists of a small *reference pinhole* in a semi-transparent membrane, placed near the focus of a coherently illuminated optical system under test. The illuminating beam is often generated by a suitable *object pinhole spatial filter* to ensure a coherent, spherical wavefront.

A single beam passes through the test optical system, acquiring the aberrations of interest here. This may be considered as the linear superposition of two beams transmitted through the pinhole membrane. One beam passes through the membrane undiffracted and forms the interferometer's *test beam*. Light diffracted through the tiny pinhole forms the *reference beam*, and overlaps the test beam across the

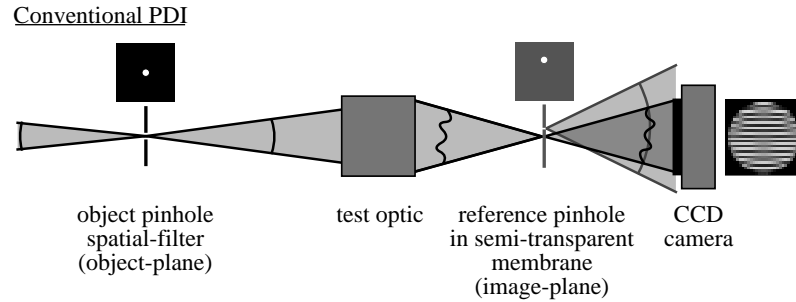


Figure 1. A schematic representation of the essential components of the Conventional PDI. A tiny pinhole in a semi-transparent membrane is placed near the focus of a coherently illuminated optical system. Light diffracted from the pinhole forms a reference wave that overlaps the test wave over the numerical aperture of interest.

measurement NA. In principle, the reference beam consists of a nearly perfect, spherical wavefront, and the test beam contains the aberrations of the optical system. Where the overlap occurs, interference fringes appear in a measurable pattern that reveals the path-length difference between the two beams.

The reference pinhole size must be chosen to balance two opposing concerns: throughput and reference wavefront quality. The pinhole should be significantly smaller than the diffraction-limited focal spot size of the optic under test to ensure a high-quality diffracted reference wavefront across the NA of measurement. Reducing its size decreases the amount of light diffracted into the reference beam. Because interference fringes are required for analysis, the pinhole often must be displaced significantly from the focus into a region where the light intensity is low. This further reduces the amount of light in the reference beam. From the balance of these considerations, the transmission of the semi-transparent membrane is chosen to provide nearly equal intensity in the two interfering beams, ensuring high fringe contrast. The optimum number of fringes required for analysis is strongly dependent on the power spectrum of the test optic. Analysis issues are addressed in Part IV.

3.3 EXPERIMENTAL COMPONENTS

This section presents a description of the key components of the EUV PDI system configured for the measurement of Fresnel zoneplate lenses. The key elements are shown schematically in Fig. 2.

3.3.1 EUV Fresnel Zoneplates

A number of zoneplates were prepared and examined with the EUV PDI. Because of experimental limitations, the wavefront aberrations were carefully investigated in only one zoneplate.

A series of similarly prepared zoneplates was fabricated by Erik Anderson and Dieter Kern (1992) for testing with the EUV PDI. The binary zoneplates used in these experiments were fabricated in electroplated nickel on a silicon-nitride membrane. The zone plates have a diameter of 200 μm , an outer zone width of 75 nm, and a *primary* or *first-order* focal length of 1.2 mm at 13.5-nm wavelength. The zone

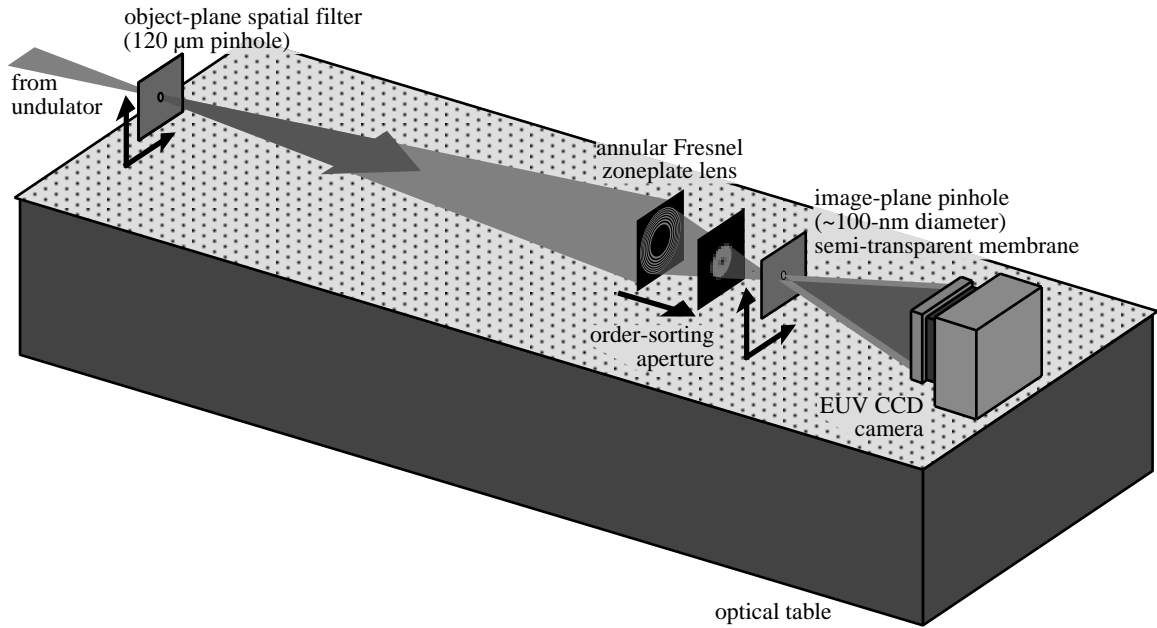


Figure 2. The arrangement of the PDI components configured for EUV Fresnel zoneplate measurement, 1994-5. The arrows indicate the degrees of freedom of the five translation stages. Measurements were performed at Beamline 9.0.1 at the Advanced Light Source.

plates contain an opaque *central stop* of 60- μm diameter, which gives them an annular pupil. Without the central stop, the zoneplate design calls for approximately 640 transparent and opaque zone pairs.

As discussed in Appendix 4, EUV light is diffracted by the zoneplate into a series of converging and diverging diffractive orders, each with a unique real (converging) or virtual (diverging) focal point. In addition to the diffracted orders, there is a strong “undiffracted” zeroth-order component that propagates forward without focusing.

Wavefront measurements are based on the focused first-diffractive order. Overlapping light from the other orders is blocked by an essential, appropriately-located aperture stop, called an *order-sorting aperture* (OSA). Of primary concern are the overlapping zeroth-order and negative-first-order beams. If not adequately blocked, the strong zeroth-order beam is capable of causing damage to a sensitive detector. Although it contains only (roughly) twice as much flux as the first-order, it propagates in a comparatively narrow angle. The negative-first-order beam is of equal strength as the first-order beam and propagates past the focus with the same divergence angle. Because these beams originate from the comparatively small zoneplate lens and propagate over a large distance, their overlap in the detector plane is nearly complete.

The OSA is placed in a position where it takes advantage of the opaque central stop of the annular pupil. This is shown in Fig. 3. It is necessary to place the OSA far enough away from the zoneplate that the first-order beam is narrower than the diameter of the OSA pinhole while maintaining enough working distance in the vicinity of the focus to allow the PDI membrane room to operate. The position of the OSA

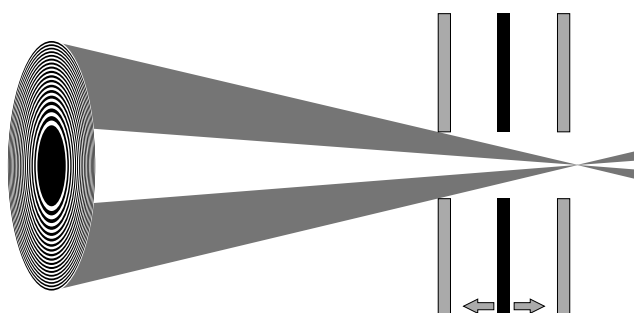


Figure 3. Position of the order-sorting aperture to transmit only the focused, first diffracted-order from a Fresnel zoneplate. With a 60 μm central stop in the 200- μm -diameter annular zoneplate and a 50- μm OSA pinhole, the OSA must be placed more than 3/4 of the distance to focus from the zoneplate; yet the OSA must not project so far as to limit access to the focal plane by the PDI pinhole membrane.

determines the range of wavelengths that can be used without obstruction. Some of the data in this chapter show the effects of the OSA encroachment on the first-order beam. With a first-order beam of 200- μm diameter at the zoneplate, and an OSA of 50- μm diameter, the OSA must be placed beyond 3/4 of the distance to focus. Here, with a focal length of 1.2 mm, the OSA must be placed beyond 0.9 mm from the zoneplate, leaving less than 0.3 mm of working distance.

The OSA is mounted to the zoneplate membrane and positioned in the following way. The OSA pinhole exists at the center of a thin, circular metal foil. Using an appropriately-sized ball-bearing, the foil is forced to conform to a spherical shape by firmly pressing the ball-bearing and foil into a thick piece of rubber. The foil then forms the shape of a spherical cap, with the pinhole at the center. The target height of the cap is around 1 mm, but not less than 0.9 mm. Using a microscope to observe the back-illuminated zoneplate, the cap is carefully positioned with the OSA pinhole above the zoneplate center. It is then held in place using a drop of epoxy.

3.3.2 Light Source Description

The light source used in these experiments is an undulator beamline operating at the Advanced Light Source (ALS) at Ernest Orlando Lawrence Berkeley National Laboratory. The beamline incorporates a spherical grating monochromator with a resolving power of $\lambda/\Delta\lambda \approx 3000$ (FWHM) at 13-nm wave-

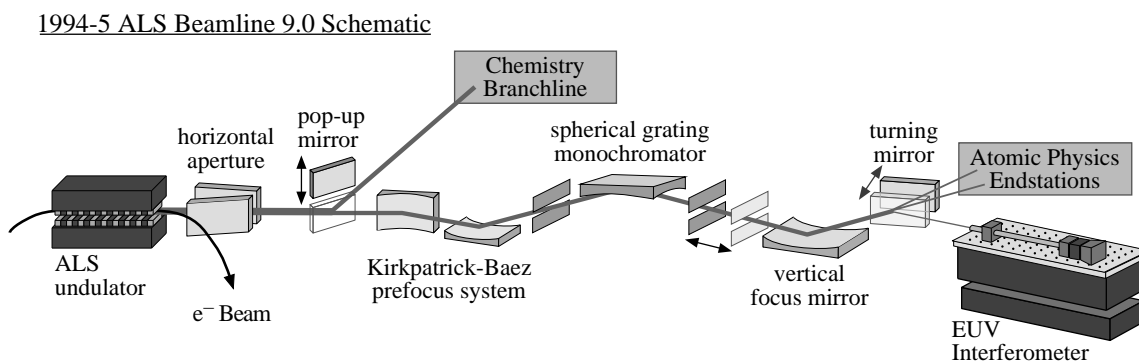


Figure 4. Schematic representation of the shared 8-cm-period undulator beamline 9.0 at the Advanced Light Source, c. 1994-5. A spherical grating monochromator provides a resolution of $\lambda/\Delta\lambda \approx 3000$ and a flux of 10 mW through a 120- μm pinhole. In the horizontal direction, the source is imaged onto the interferometer's object plane, 1:1. A bendable focusing mirror vertically re-images the beam from the monochromator's exit slit onto the interferometer's object plane.

length. Glancing incidence beamline optics, shown schematically in Fig. 4, focus the beam both horizontally and vertically onto an entrance pinhole spatial filter located 2.4 meters from the zone plate. The entrance pinhole diameter, which determines the spatial coherence of the zoneplate illumination, was chosen as 120 μm to maximize throughput without sacrificing illumination uniformity. This diameter is small enough that the zoneplate produces a diffraction-limited focal spot with a central Airy disk diameter of approximately 170 nm in the plane of the primary (first-order) focus. Flux through the entrance pinhole is in the range of 10^{11} – 10^{12} photons per second, or ~ 10 μW at 13.0-nm wavelength, depending on experimental conditions, including wavelength and other beamline settings.

3.3.3 Pinhole Descriptions

A variety of image-plane reference pinholes were fabricated for use in the first EUV PDI experiments. As this was a prototypical system, the optimal pinhole membrane configuration was not known before the experiments were conducted. Special membranes were fabricated (Spallas et al. 1995) containing an array of pinhole sizes and with a graded absorber thickness, according to the prescription of Sommargren and Hostetler (1993). These arrays were intended to cover a range of testing situations and also to identify the optimum experimental combination of attenuation and pinhole size. The original design of this membrane, shown in Fig. 5, consisted of a 200-nm-thick silicon-nitride membrane and a graded cobalt film of approximately 40 to 70-nm in thickness as the absorber layer. The pinholes, patterned by electron beam lithography, ranged in size from 150 to 400-nm in diameter. The pinholes were etched completely through the silicon-nitride membrane prior to the cobalt deposition. This thermal evaporation process was done using care to achieve highly anisotropic deposition, which maintains the open pinholes through both the cobalt absorber and the silicon-nitride membrane.

Initial PDI interferometric tests (Goldberg et al. 1994, 1995a, 1995b) revealed that to improve the reference wavefront quality and fringe contrast, smaller pinholes and increased attenuation were required. Both objectives were satisfied by an additional deposition step. Approximately 2.4 nm of chromium, followed by 24 nm of gold, were deposited by thermal evaporation. The effective pinhole diameters were determined before and after deposition by observation of the diffraction pattern, including angles beyond the angle of the first diffraction minima, under plane-wave illumination conditions. Pinhole diffraction data is described in Section 3.5.

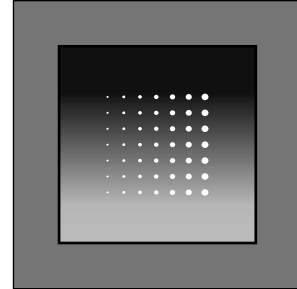


Figure 5. The PDI pinhole array provides a range of pinhole diameters and absorber thicknesses for various working conditions. The pinholes, spaced by 40 μm , are used one-at-a-time.

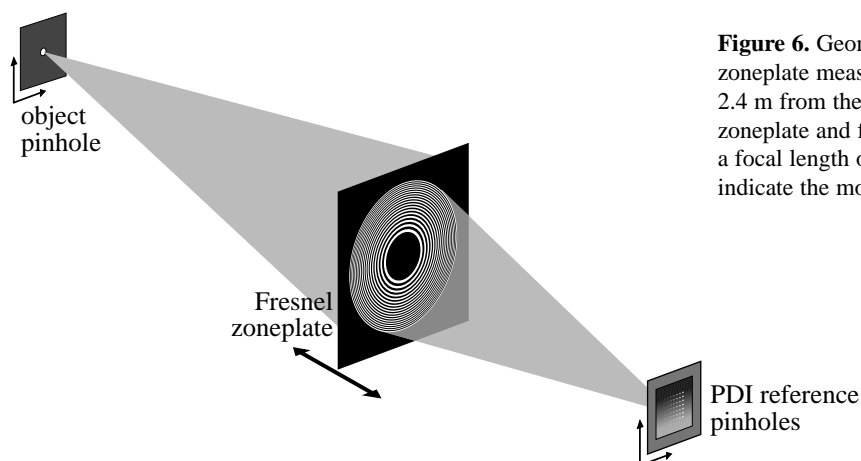


Figure 6. Geometry of the PDI Fresnel zoneplate measurement. The object pinhole, 2.4 m from the zoneplate, is imaged by the zoneplate and forms a first-order focus with a focal length of 1.2 mm at 13 nm. Arrows indicate the motions of the five stages.

3.3.4 Stages

Alignment of the essential components of the interferometer is achieved using five translation stages, shown in Fig. 6. The object pinhole spatial filter sits on a kinematic rotation stage, allowing it to be easily removed and replaced. This is mounted to a two-axis lateral translation stage, controlled by hand using two micrometers. The system demagnification of 2000 and the relatively large pinhole size (120- μm) make hand-positioning possible. Positioning the reference pinhole near the zoneplate focus requires three degrees of freedom. Here the zoneplate is mounted to the end of a cylindrical tube that attaches snugly into an axial mount maintaining a constant polar-angular orientation. Through a pair of bellows, this mount is coupled to a longitudinal-direction stage outside of the vacuum chamber. The PDI pinhole membrane attaches kinematically to a mount that is also coupled through a bellows to a high-resolution lateral motion stage. Using a pair of dc-motors and a two-dimensional Heidenhein scale, this critical stage is capable of 0.01- μm resolution and stability over an approximate area of 8 mm \times 2 mm.

3.3.5 Other Components

At a distance of several centimeters beyond focus, the light from the zeroth-order beam is hundreds of times more intense than that of the first diffracted order. While the first-order beam diverges to a diameter of 2 cm at the CCD detector plane, the zeroth-order beam remains approximately 200 μm wide. Hence the intensity per unit area is 10,000 times higher in the zeroth-order than the first. To protect the sensitive CCD detector from accidental misalignment of the OSA, a small circular beam-stop is placed before the CCD detector. This beam-stop, often referred to as *the lollipop*, is held by two thin, adjustable wires. Its shadow is visible as a grey disk in the center of each image.

The CCD detector used in these experiments is a Princeton Instruments 1024 \times 1024 pixel, back-thinned, back-illuminated, 1-square-inch area, 16-bit detector. At 13.4-nm wavelength, the CCD sensitivity is approximately 0.8 measured counts per photon (measured by Patrick Naulleau). This value is based on measurement of the statistical distribution of measured intensity values at various illumination levels. To

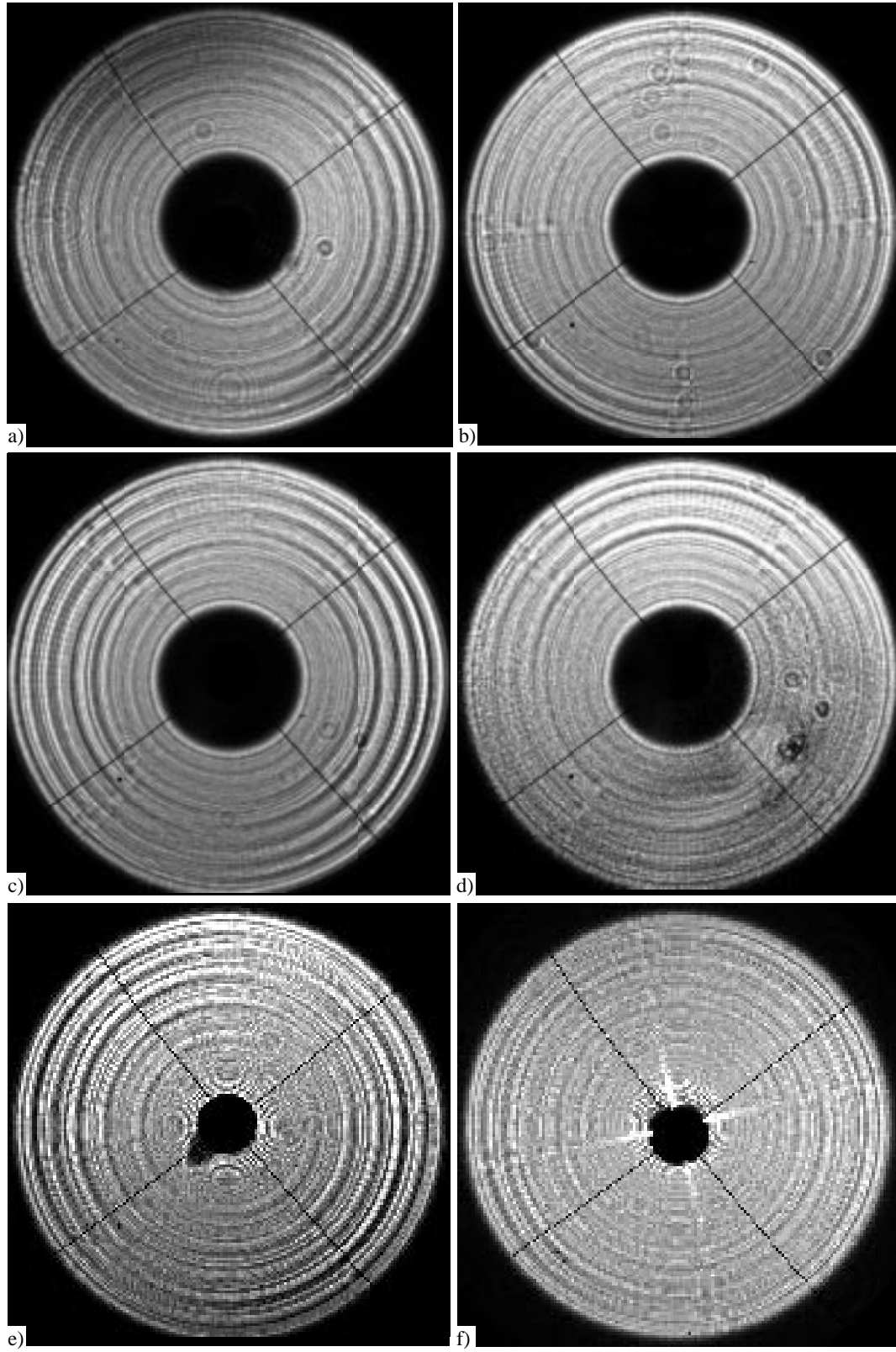


Figure 7. Six separate Fresnel zoneplates were inspected with EUV light. (a) through (d) are made of the same annular design, while (e) and (f) are made with no central stop region. The inspection wavelength is as follows: (a) 12.4 nm (100 eV); (b) through (e) 13.48 nm (92.0 eV); (f) 11.64 nm (106.5 eV). Only zoneplate (a) was used extensively in wavefront measurements.

reduce the contribution of *dark noise*, the detector is cooled to temperatures below -30°C during the experiments. To protect the CCD from contamination, a square-ring cryo-pump *cold-finger* in thermal contact with a liquid nitrogen bath is placed in close proximity to the detector.

A differential ion pump separates the interferometry endstation from the vacuum system of the beamline. Turbo pumps are used to maintain pressures below 1×10^{-5} torr.

3.4 THE TEST WAVE: FRESNEL ZONEPLATE DIFFRACTION PATTERN

Under uniform illumination conditions, the stationary test wavefront measured in the detector plane (far-field) resembles the illumination pattern of the pupil. A 120- μm -diameter pinhole spatial filter placed 2.4 m from the annular Fresnel zoneplate lens provides coherent illumination of acceptable uniformity: at 13.0-nm wavelength, the first Airy-null in the pupil plane has a radius of approximately 300 μm . The radius of the zoneplate is only 100 μm .

The diffraction patterns from a number of similar zoneplates were inspected. Figure 7 shows six of these images. In each case, mid- and high-spatial-frequency errors are clearly visible as circular and radial features in the images. These effects are the result of small fabrication errors, either in zone-placement or in the line-to-space ratio (Tejnil et al. 1996b).

3.5 THE REFERENCE WAVE

The accuracy of the PDI is primarily determined by the quality of the spherical reference wavefront, which is largely determined by the size of the reference pinhole. Size is the most critical aspect of the PDI reference pinholes: they must be small enough to diffract a high-quality spherical wavefront overlapping the entire NA of the zoneplate. Open pinholes on the order of 100-nm diameter in a thick, absorptive membrane are extremely difficult to fabricate, and more challenging to procure. Often the pinholes used in these experiments were slightly larger than the target size range.

Using EUV light, the pinhole quality was established in three ways: first, by inspection of a sampling of pinholes with electron-beam microscopy; second, by observation of the independent pinhole dif-

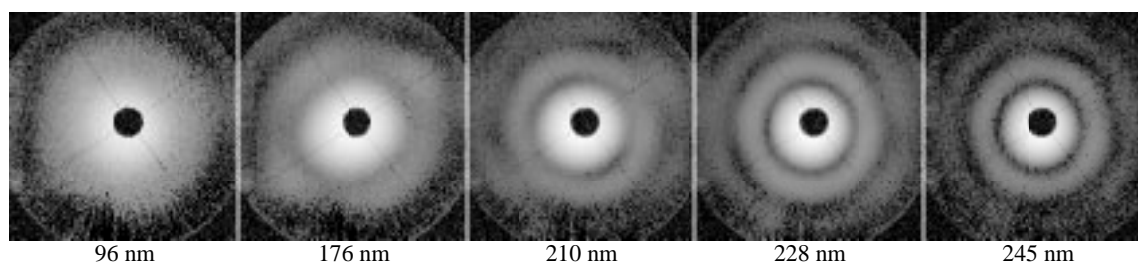


Figure 8. Measured pinhole diffraction patterns from five adjacent reference pinholes of different size. The circular Airy-like diffraction minima enable estimation of the pinhole diameters, as shown below each pattern. The shadow of a small, round beamstop suspended close to the CCD detector is visible as a dark disk in the center of each image.

fraction pattern; and third, by inspection of the measured interferograms. The following sections describe these observational procedures and enumerate the most important experimental difficulties. The issues discussed here are the critical size of the reference pinhole and the inadvertent contamination of the semi-transparent membrane during experiments.

3.5.1 Pinhole Diffraction

One way to characterize the pinholes and the reference wavefront *in situ* is to perform pinhole diffraction experiments in which isolated reference pinholes are uniformly illuminated and the far-field diffraction pattern is observed. In order to perform this experiment, a 50- μm diameter circular aperture was placed within 5 mm of the pinhole membrane. In this configuration, with no optical system (zoneplate) in place, the diffraction pattern from each reference pinhole of the 7×7 array was measured at 12.4-nm wavelength.

Five diffraction patterns representing one row of pinholes with increasing diameter and constant absorber thickness are shown in Fig. 8. These pinholes were located in the thickest part of the absorber substrate. The approximate effective pinhole sizes are calculated from diameters of the first minimum ring of the Airy-like diffraction patterns.

3.5.2 In Situ Pinhole Size Assessment

It is important to develop inspection criteria to distinguish unacceptable pinholes *in situ*. There are several rapidly identifiable clues in the data which serve as warnings of poor pinhole quality. Usually the interference fringe pattern reveals a clear signature of the reference wavefront. Under uniform plane-wave illumination conditions, the expected diffraction pattern of the reference wave is the well-known Airy-pattern of concentric circular rings surrounding a bright central lobe, and separated by circular intensity nulls. A uniform wavefront phase in each of these rings is shifted by π radians from the neighboring rings. When the pinhole is placed in the outer regions of the focal pattern of the test optic, where the reference pinhole illumination is rapidly-varying, the pinhole diffraction pattern can no longer be described simply as an Airy pattern; yet it does contain many of the same features.

Note: a common practice during the zoneplate experiments is to perform a *background subtraction* to improve the fringe visibility. Here, an image of the test beam alone is acquired with the reference pinhole located very far from the focused beam. By subtracting the test beam pattern from subsequent measurements, the average intensity is close to zero and even faint fringes became clearly visible. The images in Fig. 9 have all undergone background subtraction.

3.5.2.1 Zeros of Fringe Visibility. Bringing the reference-pinhole-containing membrane out of the focal plane yields an interference pattern of concentric rings. These *defocus* rings result from the mismatched radii-of-curvature of the test and reference beams. It is easily shown from the Fresnel diffraction integral (Goodman 1988:59-60) that for a small longitudinal displacement z , the number of waves of defo-

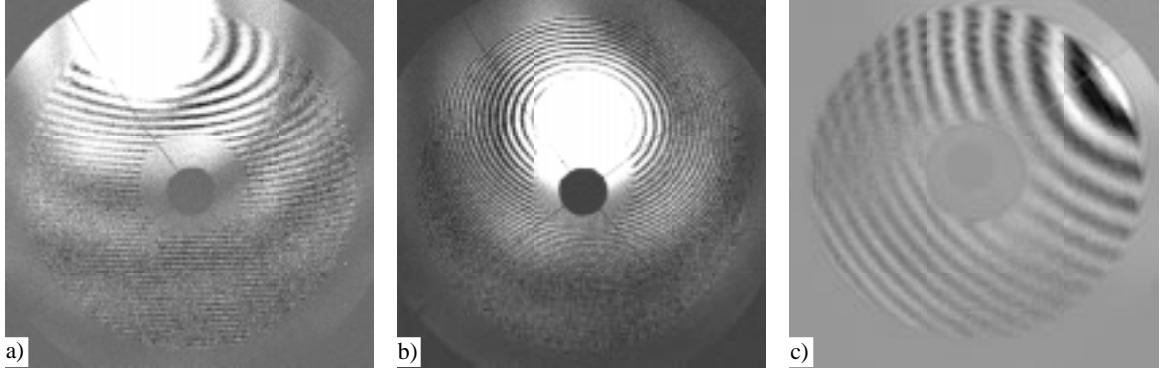


Figure 9. (a) and (b) Interferograms from over-sized reference pinholes show clear evidence of reference wavefront intensity minima within the NA of measurement. When the system is out of focus, the broad reference wave intensity patterns are clearly visible as a modulation in the fringe contrast. (c) Although less pronounced here, the loss of fringe contrast is from this same effect.

cus (equivalent to the number of fringes observed) is

$$n = \frac{(NA)^2 z}{2\lambda} \Rightarrow 4.1 \mu\text{m} / \text{fringe at } 0.08 \text{ NA, } \lambda = 13.0 \text{ nm} . \quad (1)$$

With a high-density of defocus fringes, reference wave intensity nulls are easily observable as circular bands of zero fringe contrast. This is evident in Fig. 9. Here the images are a combination of multiple patterns: the slowly-varying bands of contrast modulation due to the large pinhole size, the rapidly-varying defocus-fringes due to the longitudinal displacement of the pinhole, the annular pupil of the zoneplate, and the shadow of the beam-stop. Wherever the reference wavefront amplitude nulls occur, the fringe contrast becomes zero. The displaced center of the ring pattern is due to a lateral displacement of the reference pinhole from the test-beam axis.

3.5.2.2 Fringe forking. An abrupt reference wavefront phase shift of π radians produces a rapid change in the fringe pattern, from bright to dark or vice-versa. This effect is here referred to as *fringe forking*. Several examples of this behavior are shown in Fig. 10.

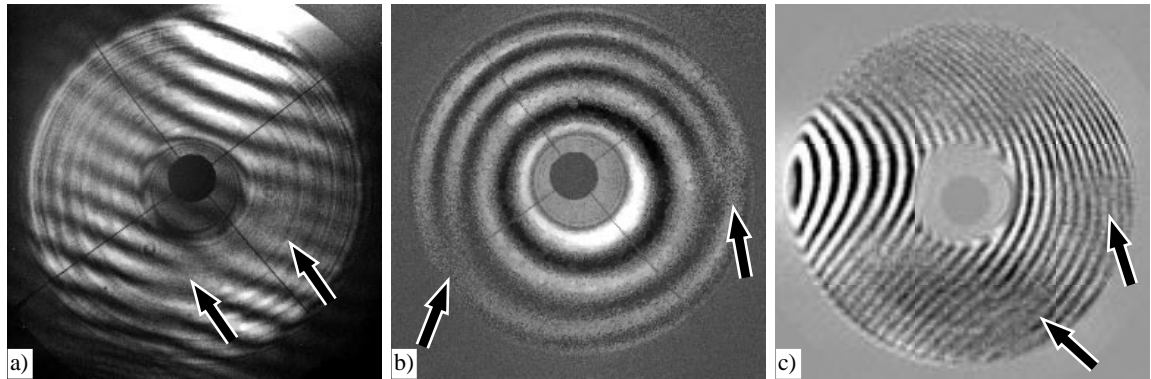


Figure 10. The presence of “forked” fringes, as indicated by the arrows, gives clear evidence for over-sized pinholes. The pinhole diffracted wavefront undergoes an abrupt half-cycle phase-shift as it crosses a diffraction minimum. This causes a point or contour of zero fringe visibility bordered by *forked* fringes one-half-cycle out of phase.

3.5.2.3 Contrast variation. Even when the pinhole is small enough that there are no regions of zero fringe visibility and no forked fringes, it may still be too large. A properly-sized pinhole behaves as a good spatial filter and creates a uniform reference wave. When an interference pattern contains any regions of reduced fringe visibility, the pinhole is still too large. Often observed are bright regions aligned in the direction perpendicular to the fringes. Most likely this is caused by the directionally-dependent illumination pattern in the focal plane: the pinhole samples a small region in a pattern of rings, causing a directionally-dependent diffracted wave to result. This effect is present in Fig. 10(c).

3.5.2.4 Contamination. One major experimental difficulty facing EUV interferometry is the issue of hydrocarbon contamination. Although it has not been well characterized, this contamination is frequently observed in varied experiments involving EUV light (Alastair MacDowell, Avijit Ray-Chaudhuri, Werner Meyer-Ilse, personal communication). Hydrocarbon contamination on otherwise clean surfaces apparently occurs at a rate which is dependent both on the density of hydrocarbons in the vacuum system, and on the local intensity of EUV light impinging on a surface.

Because it relies on diffraction from a tiny object in the image-plane, the PDI is *very sensitive* to imperfections in the semi-transparent pinhole membrane — especially those that are close to the reference

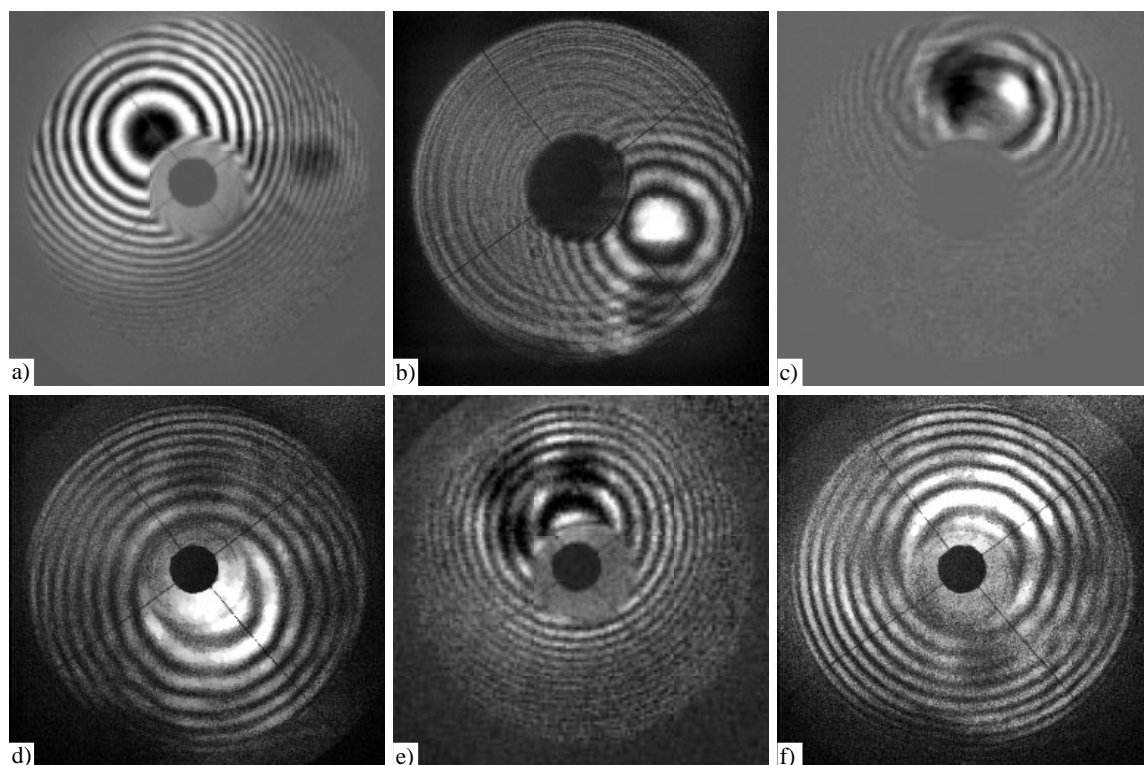


Figure 11. Mask contamination, damage, or defects greatly impair the proper use of the EUV PDI. System alignment and interferogram-recording with long, continuous exposure times inadvertently damaged the mask in the vicinity of the reference pinhole. (d) through (f) Damage is often concentrated along the vertical and horizontal directions because efforts were made to record interferograms with horizontal and vertical fringe patterns. Evidence of this damage is pronounced in the defocused interferogram patterns shown here.

pinholes. Any non-uniformity, transparent or opaque, behaves as an additional point-diffractor corrupting the quality of the reference wavefront. The most sensitive component of the PDI, the pinhole membrane, also receives the most strongly focused EUV light, making it highly vulnerable to contamination. Long, continuous exposures during the interferometry experiments and the inspection of reference pinholes severely damaged many of the membrane pinholes used in these experiments.

Evidence of this damage is clearly visible in the interferograms shown in Fig. 11. In many of the interferometry experiments an attempt was made to align the fringes with either a horizontal or vertical orientation. To do so implies that the reference pinhole must be displaced horizontally or vertically from the center of the focal pattern. Many of the observed damage patterns (especially Figs. 11(c) through (e)) display a “+” pattern consistent with the deposition of hydrocarbons along the two axes. When the pinhole membrane is displaced from the focal plane by several microns in the longitudinal direction, a larger area of the membrane is illuminated. Hence, contamination features that are (relatively) far from the reference pinhole contribute to the interference pattern.

More evidence of contamination in the mask can be seen in the interferogram data of Section 3.6. When, because of contamination, there is more than one point-diffractor, and thus more than one “filtered” reference beam, the multiple beams combine to form an interference pattern of their own, separate from the test wavefront. For example, in the center of the annular aperture where the test beam intensity is nearly zero, a fringe pattern is often observed. Because these multiple “reference beams” are spatially filtered, they typically cover the entire measurement NA, and their interference is most noticeable in the dark regions of the pattern. When image subtraction is used to remove the unmodulated portion of the intensity pattern, these separate, fainter patterns of reference wave interference are most visible.

Two successful, proven ways to combat the build-up of carbon contamination are, first, to clean the experimental and vacuum system components to remove latent sources of hydrocarbons (finger-prints, grease, etc.), and second, to introduce a small pressure of oxygen gas. Although the introduction of oxygen to the PDI system through a thin capillary aimed directly onto the pinhole membrane made no noticeable difference to the contamination issue, the beneficial effects of oxygen have been dramatically demonstrated in the PS/PDI system that followed.

3.6 PDI EXPERIMENTS

During the course of the EUV PDI experiments with the Fresnel zoneplate test optic, several data sets were collected. The limited scope of these experiments results from the narrow experimental window of opportunity that existed between the fabrication of adequately small reference pinholes and the contamination of the pinhole membrane.

Table 1. Measurement of a Fresnel zoneplate test optic in three data sets.

Data Set	Series A	Series B	Series C
Photon Energy	96.0 eV	96.0 eV	96.0 eV
Wavelength, λ	12.9 nm	12.9 nm	12.9 nm
# of images	5	5	4
Orientation	0°	139.5°	139.5°
Exposure Time	60 s	120 s	120 s
Spatial Filter	<i>none</i>	120 μ m	120 μ m
Fringe orientation	horizontal	vertical	horizontal

Among the interferometric data are three sets in particular, A, B, and C, described here and shown in Fig. 12. Each separate set represents a sequential series of images recorded with the same experimental conditions, differing only in the lateral position of the reference pinhole. In principle, an entrance pinhole spatial filter *must* be used to ensure the coherent illumination of the zoneplate test optic. However, to increase the photon flux (reduce the exposure time) and investigate the effect of the spatial filtering, interferograms were occasionally recorded without a spatial filter. Series B and C were recorded using the 120- μ m-diameter object pinhole spatial filter. For Series A, no spatial filter was used. Between Series B and C the reference pinhole was translated laterally by several microns to change the fringes from horizontal to vertical; otherwise all other experimental conditions were maintained. The parameters of each series are given in Table 1.

Wavelength. The wavelength was chosen based on the fixed position of the OSA with respect to the zoneplate lens. Outside of a narrow wavelength range, the edge of the first-order beam becomes clipped by that aperture.

Intensity. The input photon flux is measured using a detector placed a few centimeters beyond the object plane. The use of an object pinhole spatial filter guarantees the coherence of the illumination at the expense of flux. Using the pinhole filter, the flux is reduced in two ways: first, the spatial filter directly limits the amount of light passing through the object plane, and second, the increased diffraction angle generated by the use of smaller pinholes sends more of the remaining light out to large angles not collected by the zoneplate. By this simple argument, the usable flux depends on the diameter as d^{-4} . In one typical measurement, a 120- μ m object pinhole reduced the photon flux to 15% of its unfiltered strength. Separately, when using the 120- μ m pinhole, the measured flux collected by the zoneplate was 25.3% of the unfiltered strength; it was 2.2% of the unfiltered amount when using a 50- μ m pinhole.

Orientation. Following Series A, the zoneplate was removed and reinstalled with a different azimuthal orientation. Based on the easily-recognizable and measurable positions of the imperfections in this particular zoneplate, the rotation angle is known to be $139.5^\circ \pm 0.5^\circ$ (estimated uncertainty). This rotation is appropriately re-introduced into the wavefront data to facilitate comparison of the three sets.

Exposure Time. The exposure time was chosen to achieve more than 100 detected counts in the

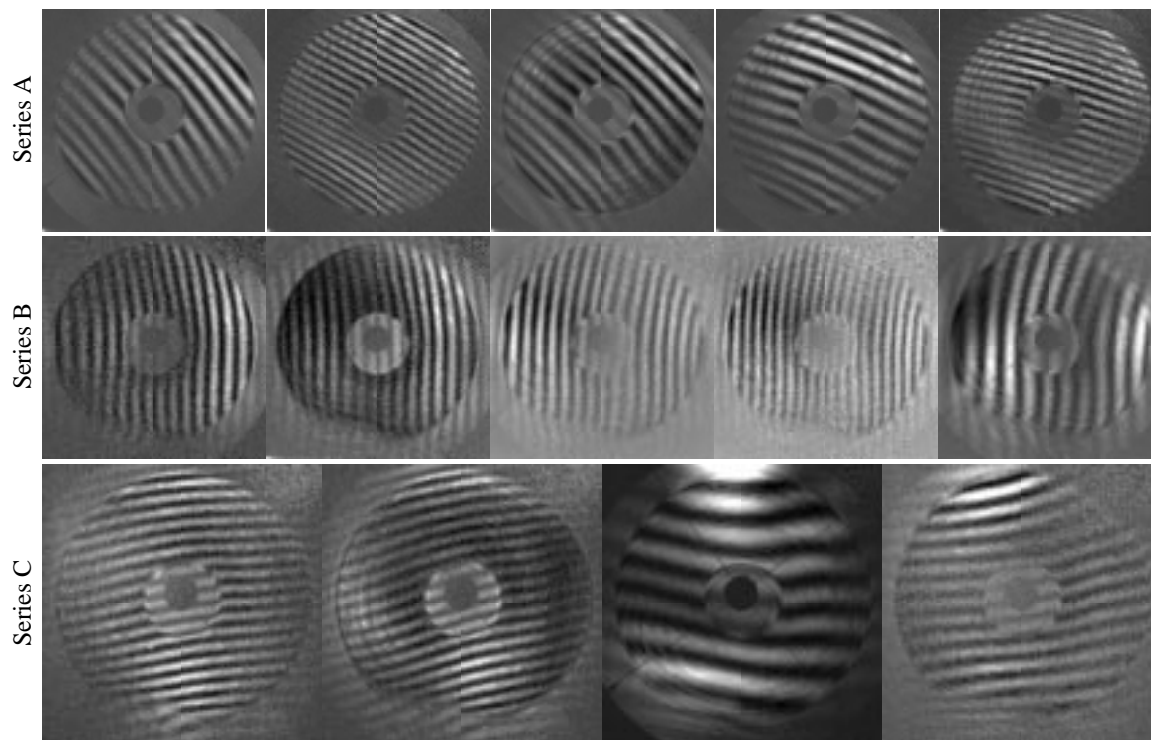


Figure 12. Three EUV interferogram data series from measurements of one annular Fresnel zoneplate lens. Series A was recorded first, when the pinhole membrane was relatively clean. Although in Series B and C the effects of pinhole membrane damage are clearly evident (non-uniform fringe contrast, fringe patterns in the dark regions of the zoneplate, etc.), the interferograms are analyzable and the wavefront may be studied.

peak-to-valley fringe modulation. This arbitrary level is a compromise between the measurement accuracy, the rate of membrane contamination, and the limited beam-time allocated for the experiments.

Alignment was performed using continuously updating exposures, each of less than two seconds in duration. To record data for future analysis, exposure times between one and two minutes were typical.

3.6.1 Raw Data

To improve the fringe visibility during system alignment and pinhole positioning, the zoneplate data were recorded using background subtraction, as described previously. The test wave images used for subtraction were recorded with the reference pinhole placed far from the focus ($20\text{ }\mu\text{m}$ away, laterally). These images are “subtracted” from subsequent images to enhance the fringe visibility during alignment and data collection.

By collecting several similar measurements in series, each analyzed individually, an attempt is made to quantify and reduce random measurement errors. Analysis methods are discussed in Part IV. In the analysis of each image, the wavefront is fit to a set of 37 Zernike annular polynomials, based on a central obscuration of 35% (chosen slightly larger than 30% to reduce the contribution of diffraction effects at the edge) (Melozzi and Pezzati 1992). The arbitrary piston and the position-dependent tilt and defocus terms are subtracted from the wavefront. Using the known measurement NA, a systematic coma

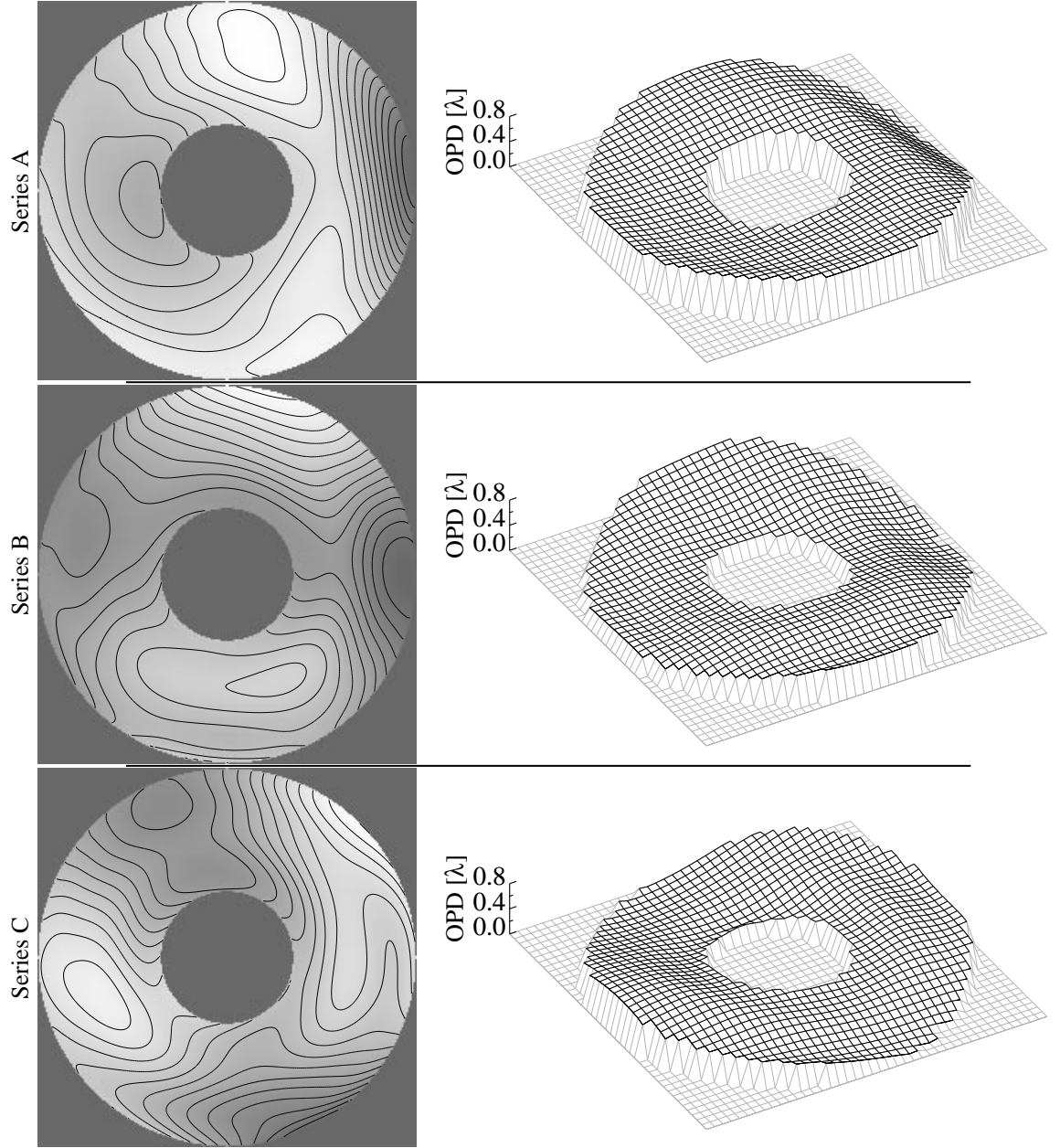


Figure 13. Contour and surface reconstructions of the averaged wavefronts from the three measurement series. Contours represent 0.05 waves, or $\lambda/20$. The azimuthal rotation angle of the Series A wavefront has been adjusted to match the angle of Series B and C.

Table 2. Global wavefront statistics for the three measurement series.						
Series	RMS			P-V		
A	0.133λ	1.72 nm	$\lambda/7.5$	0.731λ	9.43 nm	
B	0.134λ	1.73 nm	$\lambda/7.5$	0.727λ	9.38 nm	
C	0.147λ	1.90 nm	$\lambda/6.8$	0.753λ	9.71 nm	

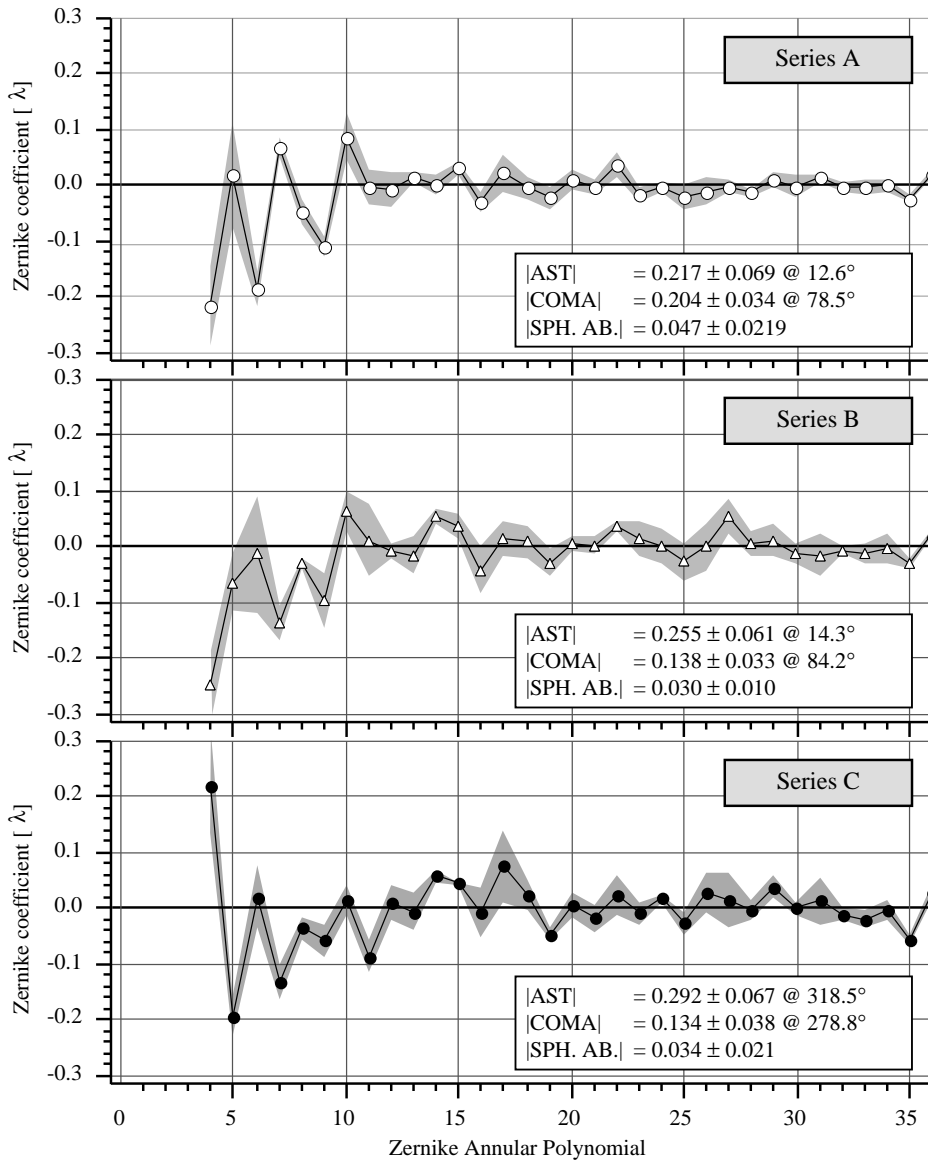


Figure 14. Zernike annular polynomial representations of the Series A, B, and C average wavefronts. The position-dependent piston, tilt, and defocus terms are not shown. The grey band behind the plot values indicates the measurement uncertainty based on the standard deviations of the data. With each plot the magnitudes and directions of the astigmatism, coma, and spherical aberration components are shown.

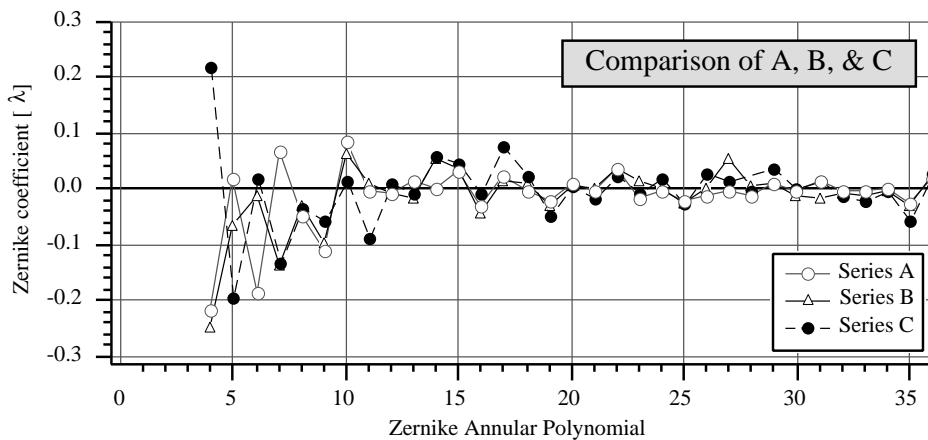


Figure 15. A comparison of the Zernike coefficients of the three measurement series. By inspection, the agreement between Series A and B is closer than between A or B and C, even though B and C were consecutive measurements.

error term is also subtracted from each set. This procedure is described in Section 5.5.2.

Contamination issues. The fringes visible in the central part of the interferograms are an indication of contamination in the PDI pinhole membrane, as described in Section 3.5.2.4. The interference of the reference wave with the light diffracted from the contamination produces these fringes, which are most easily identifiable in the regions where the test wave intensity is small. However, this interference must also span the entire NA, adding uncertainty to the measurements.

One way to estimate the amplitude of the wave diffracted from the contamination is to compare the fringe modulation in the two regions. Since the reference wave amplitude is the nearly the same in both regions, the difference in the fringe modulations reveals the relative amplitudes of the test wave and the “contamination” wave. (See Section 3.8 for a description of this method.) Based on this simple approach, the contribution of the contamination has an amplitude of approximately 1/10-th of the primary interference pattern. Hence, the contamination contributes not more than ± 0.1 radians, or ± 0.016 waves (0.21 nm, or $\sim \lambda/63$), to the phase measurements.

3.6.2 Wavefront Analysis

For each of the three data sets, the average wavefront is computed and displayed in Fig. 13. Here the wavefronts are represented in two ways, both as surface phase maps and as contour plots. Another representation of the wavefront data is shown in Figs. 14 and 15 in terms of the set of 37 Zernike annular polynomials. (This plotting format is discussed in Appendix 7.) Since the polynomial fit coefficients are calculated separately for each interferogram, a measure of the uncertainty in each term is available in the standard deviation. Each term in the plot a_n is the average of the measured coefficients; the standard deviation σ_{a_n} is indicated by the grey region. The global statistics for the three average wavefronts are shown in Table 2. Although there are qualitative differences in the measurements, these global statistics are in excellent quantitative agreement.

3.7 CONCLUSION

Several conclusions can be drawn from the interferometric zoneplate wavefront measurements described here. Foremost is the conclusion that from this high quality zoneplate, the wavefront aberrations are smaller than or on the same order as the resolution of the measurements. *Within* each series the uncertainties are low relative to the comparison of the three. This means only that the wavefront measurements were reproducible in a very limited way — a change of the experimental geometry affected the outcome of the test. The primary explanations for this are the poor spatial filtering capabilities of the over-sized reference pinholes, and the difficulties caused by the contamination of or damage to the reference pinhole membrane.

These tests represent some of the first at-wavelength wavefront measurements performed on high-

resolution EUV optics, and are the first using a point diffraction interferometer. At the time they were conducted, they demonstrated the ability to measure sub-wavelength aberration magnitudes. Further progress on the development of the EUV PDI was arrested by the invention and implementation of the PS/PDI, which is in many ways a superior tool.

3.8 NOTE: THE CONTRIBUTION OF CONTAMINATION TO WAVEFRONT MEASUREMENTS

To determine the effect of the waves diffracted by the mask contamination, consider a simplistic model of the interferogram intensity pattern that is composed of three waves: the test wave T , the reference wave R (of comparable magnitude to T), and a small contribution from the light diffracted from the contamination c . The intensity pattern may be written as follows using three arbitrary phase functions:

$$I = |T + R + c|^2 = |T|^2 + |R|^2 + |c|^2 + 2|TR|\cos\phi_1 + 2|Tc|\cos\phi_2 + 2|Rc|\cos\phi_3. \quad (2)$$

This simplifies to a stationary intensity A , plus the modulation terms from the three cross-products.

$$I = A + 2|TR|\cos\phi_1 + 2|Tc|\cos\phi_2 + 2|Rc|\cos\phi_3. \quad (3)$$

Outside of the main illuminated area, where the test wave amplitude is small ($T \approx 0$) and the reference wave overlaps the contamination wave, the total peak-to-valley fringe height is

$$I_{small} \approx 4|Rc|. \quad (4)$$

In the *main region* of the interferogram, the pattern is dominated by the interference of the test and reference waves.

$$I_{large} \approx 4|TR|. \quad (5)$$

The ratio of the fringe heights in the two areas allows us to estimate the relative amplitude of the contamination wave.

$$\frac{I_{small}}{I_{large}} \approx \frac{4|Rc|}{4|TR|} = \left| \frac{c}{R} \right|. \quad (6)$$

Based on the addition of the two complex waves c and R , within this simple model the wavefront phase uncertainty, in radians, is given by this ratio.